CHAPTER-2

A Peroxidase-Mimicking Single Amino Acid Bionanozyme for Ultrasensitive Biomarker Detection: A WHO-REASSURE-Aligned Approach

2.1 Introduction

The advancement of biosensing technologies, adhering to the REASSURE (Real-time connectivity, Ease of specimen collection, Affordable, Sensitive, Specific, User-Friendly, Rapid and Robust, Equipment free or simple Environmentally friendly, Deliverable to end-users) criteria set by the World Health Organization (WHO), holds considerable promise for application in resource-limited settings.[1,2] These technologies are expected to have a profound impact on biomedical diagnostics, food safety, and environmental monitoring. One particularly fascinating area of focus is the development of biosensors specifically designed to detect important biomarkers such as hydrogen peroxide (H_2O_2) [3,4], Dopamine (DA) [5], and Nitrite ion (NO_2^-), ions.[6,7] H_2O_2 is known for its powerful oxidizing characteristics, which can present serious health risks through various exposure routes. Meanwhile, DA, a vital neurotransmitter, is closely linked to neurological functions, and fluctuations in its levels can be associated with conditions like Parkinson's and Alzheimer's. Additionally, accurate detection of nitrite (NO_2^-) levels in food items is crucial for preventing health risks associated with overconsumption, given that $NO_2^-$is commonly used in food preservation.[8,9] Hence, the development of advanced biosensors for detecting H_2O_2, DA, and NO_2^- not only promises to improve disease monitoring but also plays a vital role in ensuring food safety and quality, ultimately leading to significant improvements in overall human health and well-being.[10] In this regard, a pivotal element in biosensing technology is the utilization of peroxidase (POD) enzymes, renowned for their ability to catalyse the oxidation of diverse substrates through the reduction of H_2O_2 **(Figure 1a).**[11] This enzymatic activity underpins the development of sensitive and selective colorimetric assays, where the oxidation products induce noticeable colour changes correlating with the concentration of target analytes.[12] Nevertheless, natural POD enzymes present several challenges.[13] They are costly to produce and purify, sensitive to harsh physical and chemical conditions, and lack operational stability. Moreover, natural enzymes pose difficulties in transferability, modification, recovery, and recyclability, necessitating the exploration of alternative biosensing methodologies. Recent advancements in nanotechnology have introduced nanozymes—nanomaterials that exhibit enzyme-like catalytic properties—as a promising solution to the shortcomings of natural enzymes.[14] Nanozymes offer several advantages, including enhanced stability and tunable catalytic activity, making them suitable candidates for biosensor development. Research efforts have primarily concentrated on replicating the functions of various oxidoreductase enzymes, such as POD, catalase, oxidase, and superoxide dismutase.[15] The pioneering work on POD-mimicking nanozymes began with the identification of Fe_3O_4 nanoparticles in 2007.[16] Subsequent studies revealed that specific

Fe^{2+}-based nanocomposites could mimic POD activity by converting H_2O_2 into O_2 and hydroxyl radicals *via* the Fenton oxidation mechanism, exhibiting comparable catalytic efficiency and low substrate affinity. Notably, functionalizing the surface of Fe_3O_4 nanozymes with bioinspired amino acids significantly improved substrate affinity through hydrogen bonding interactions **(Figure 1b).**[17] To overcome the stability issues and narrow pH range activity of Fe^{2+}, researchers have explored the use of Cu^{2+} ions in developing POD-mimicking nanozymes via the Fenton-like reaction.[18,19] Despite these advancements, most nanozymes are inorganic-based nanomaterials, which significantly differ from the complex structure and properties of natural enzymes. This discrepancy hinders a thorough understanding of the enzymatic mechanisms and limits the rational design of artificial enzymes with predictable functionalities.[20] Additionally, the biomedical applications of these nanozymes are constrained by demanding synthetic conditions, complex fabrication processes, expensive equipment, toxic nature, and low specificity.

In response to these challenges, the development of bioinspired *de-novo* designed catalytic biomolecular nanoassemblies, or bionanozymes, has emerged as a promising avenue.[21–23] Bionanozymes utilize biomolecules as building blocks, often in conjunction with cofactors, to mimic the structure and function of natural enzymes. This approach offers several advantages. Firstly, the utilization of biomolecules enables the creation of bionanozymes with structures that closely resemble those of natural enzymes, potentially facilitating a more accurate understanding of enzymatic mechanisms.[24] Secondly, the design of bionanozymes can be more precise, allowing for the creation of artificial enzymes with specific functionalities tailored for desired applications. Significant progress has been made in developing peptide-based bionanozymes that replicate the active sites and catalytic features of various enzymes [25]. Recent research has notably demonstrated the development of cofactor-free peptide assemblies exhibiting POD-mimicking biocatalytic activity **(Figure 1c).**[26,27] Understanding the catalytic mechanisms of these bionanozyme systems is crucial for elucidating the structure-function relationships of natural enzymes and for the rational design of more efficient artificial enzymes. Building on these advancements, our research focuses on a further minimalistic approach to bionanozyme design.[28] Herein, we describe the development of the simplest F-Cu bionanozyme that utilizes easily available and environmentally friendly single amino acid, phenylalanine (F), coordinated with Cu^{2+} ions to form ultrathin, 2D hierarchical layered crystals **(Figure 1d).** This simplest design leverages the redox-active (Cu^{2+}/Cu^{1+}) sites, making it a promising candidate for mimicking POD activity. Furthermore, we investigate the POD-

like biocatalytic performance of the F-Cu bionanozyme and demonstrate its potential for developing WHO-REASSURE criteria-aligned ultrasensitive colorimetric sensing platforms for H_2O_2, DA, and NO_2^-.

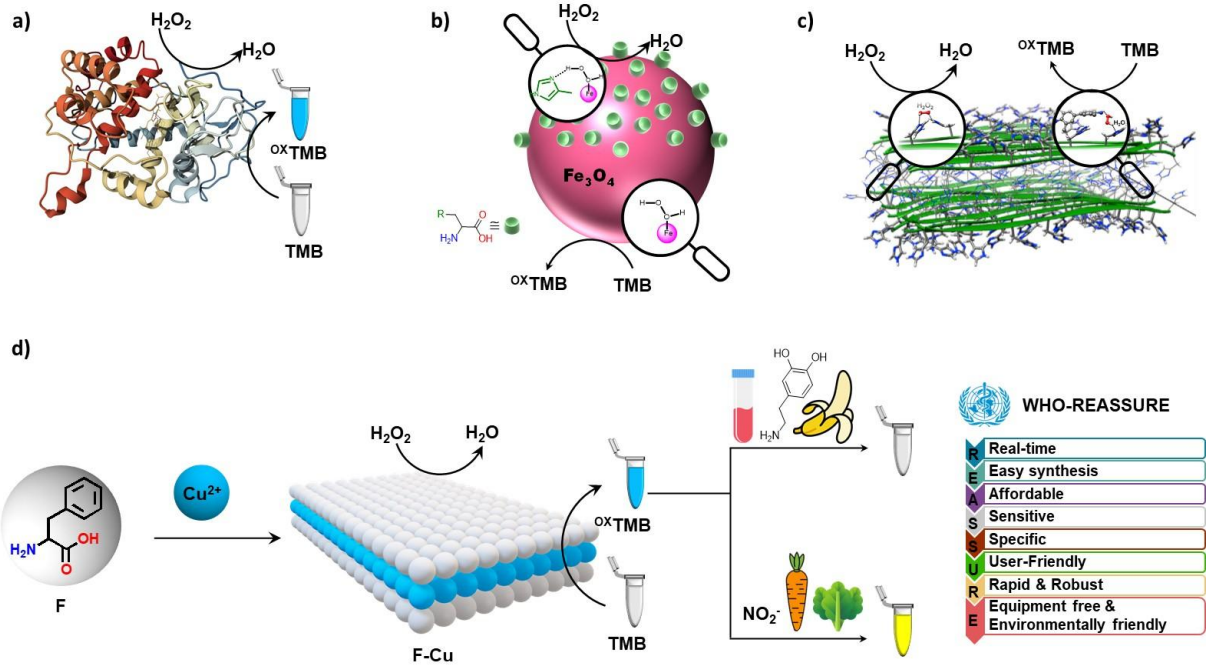

Figure 1. **(a)** Structure and biocatalytic function of peroxidase (POD) enzyme (PDB: 1GZA; contains 344 amino acid protein sequence). **(b)** and **(c)** presents previously reported POD mimicking amino acid-functionalized Fe_3O_4 nanozyme and cofactor-free bioinspired peptide-based bionanozyme. **(d)** Schematic illustration of the development of single amino acid bionanozyme (F-Cu) presented in this report, showcasing its POD mimicking biocatalytic activity and its deployment as a colorimetric tool for biomarker detection, including H_2O_2 and DA (both test and real samples such as human blood serum, ripe banana peel) and NO_2^- ions (both test and real samples of spinach and carrot extracts) in accordance with WHO-REASSURE criteria.

2.2 Results and Discussion

2.2.1 Synthesis and Characterization of F-Cu Bionanozyme

The facile synthesis of a minimalistic POD-mimic was demonstrated by combining phenylalanine (F) with redox-active copper ions (Cu^{2+}) and examining the co-assembly process **(Figure 2a).** Notably, the initial interaction of F with $CuCl_2$ transformed the colorless alkaline reaction mixture into an intense blue solution, leading to the formation of blue-colored two-dimensional (2D) crystals at the air-water interface. This transition was further analyzed through the UV-visible absorption spectra of the $CuCl_2$ aqueous solution, revealing a broad visible absorbance band at 820 nm. In contrast, F alone did not present significant visible bands, as shown in **Figure 2b.** However, the aqueous solution mixture of $CuCl_2$ and F exhibited a notably more intense, broader absorbance band, with a maximum wavelength (λ_{max}) at 615 nm.

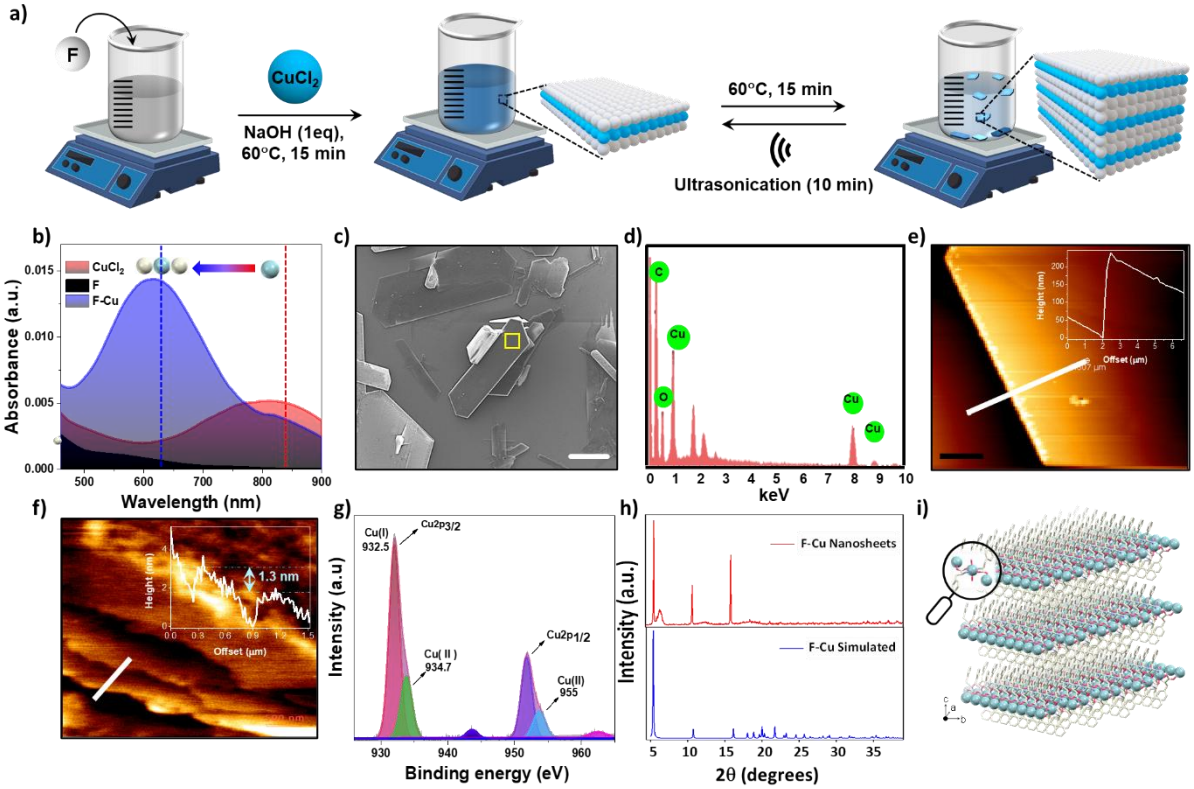

Figure 2. (a) Schematic illustration of the synthesis of F-Cu bionanozyme. **(b)** UV-visible absorption spectra of before and after (F-Cu) mixing of F and $CuCl_2$. **(c)** HRSEM micrographs of F-Cu 2D microcrystals (scale bar 500 mm). **(d)** EDX analysis on the selected area (yellow box in c) of the F-Cu microcrystal. **(e)** AFM micrographs of pristine F-Cu 2D microcrystal and its height profile. **(f)** AFM micrographs of ultrasonication-treated few layered F-Cu 2D nanosheets and their height profile. **(g)** High-resolution XPS spectra of F-Cu nanosheets. **(h)** Comparison of simulated PXRD patterns of F-Cu crystals with experimental PXRD of F-Cu nanosheets. **(i)** The single-crystal X-ray structure of F-Cu crystal shows a layer-by-layer framework held together by interlayer van der Waals forces.[20]

This pronounced shift to a higher energy band at 615 nm, accompanied by a significant blue shift ($\Delta\lambda_{max}$ = 205 nm) relative to $CuCl_2$ alone, implies the induction of a t_{2g}-e_g transition through F-Cu complexation, characteristic of octahedral copper complexes undergoing tetragonal distortion attributable to the Jahn-Teller effect. Further insights into the morphology and composition of the synthesized F-Cu were obtained through high-resolution scanning electron microscopy (HRSEM) analysis of the drop-cast F-Cu complex solution, revealing the presence of 2D microcrystals **(Figure 2c)**. Complementary energy-dispersive X-ray (EDX) analysis confirmed the integration of copper (Cu) along with carbon (C), nitrogen (N), and oxygen (O) **(Figure 2d)**. Atomic force microscopy (AFM) topographic analysis provided a detailed view, showcasing multilayered hierarchical 2D sheets spanning several micrometers in both length and width, with an average height of 230 nm **(Figure 2e)**. Subsequent

ultrasonication treatment yielded exfoliated few-layered 2D nanosheets, characterized by a single sheet thickness of approximately 1.3 nm **(Figure 2f)**. To delve deeper into the chemical composition and oxidation state of copper within the F-Cu 2D nanosheets, X-ray photoelectron spectroscopy (XPS) was employed. The high-resolution XPS spectrum elucidated peaks at 932 eV and 951.8 eV, corresponding to the Cu $2p_{3/2}$ and Cu $2p_{1/2}$ electrons of Cu^{2+}, respectively **(Figure 2g)**. Notably, the appearance of lower binding energy peaks at 932.5 eV and 955 eV signaled the presence of Cu^{+} (or Cu^{0}). Furthermore, the powder X-ray diffraction (PXRD) patterns of the synthesized F-Cu nanosheets exhibited significant congruence with the simulated PXRD patterns of F-Cu single crystals, indicating a similarity in crystallographic packing structures **(Figure 2h)**.[20] Intriguingly, single-crystal X-ray crystallographic analysis revealed a graphite-like hierarchical infinite in-plane 2D F-Cu coordinated layer-by-layer framework, meticulously held together by interlayer van der Waals forces **(Figure 2i).**[20]

2.2.2 POD Mimicking Catalytic Characterization of F-Cu Bionanozyme and its REASSURE aligned detection of H_2O_2.

Two-dimensional (2D) layered nanomaterials have long been recognized as exceptional candidates for catalytic applications due to their unique structural and electrical properties.[29] In this study, we explored the POD-mimicking biocatalytic activity of F-Cu nanosheets in the presence of hydrogen peroxide (H_2O_2) by evaluating the oxidation of the benchmark POD substrate, 3,3′,5,5′-tetramethylbenzidine (TMB). As illustrated in **Figure 3a,** the catalytic reduction of H_2O_2 by F-Cu bionanozyme converts it into H_2O molecules, during this process the colorless TMB oxidizes to a deep blue chromogenic product (^{ox}TMB) with a characteristic absorbance at 652 nm.[30] In contrast, control substrate solutions (H_2O_2, TMB, F-Cu alone, and combinations of H_2O_2+TMB, H_2O_2+F-Cu, and TMB+F-Cu) did not exhibit any significant visible color change or absorbance band, indicating the absence of background reactions **(inset photograph, Figure 3b).** Next, POD experiments have been performed in the acetate buffer as well, interestingly results suggested the more activity in PBS buffer as compared to acetate buffer **(Figure 3c)**. To determine the optimal pH for catalysis, the F-Cu catalytic assay for H_2O_2 reduction was performed at various pH levels from 1 to 9 **(Figure 3d).** The highest relative activity was observed at pH 3. As pH increased from 4 to 9, the catalytic activity of the F-Cu bionanozyme progressively decreased, indicating that an acidic environment with a pH of 3 is optimal for H_2O_2 reduction. This demonstrates the pH-dependent catalytic activity of the F-Cu bionanozyme at pH 3.

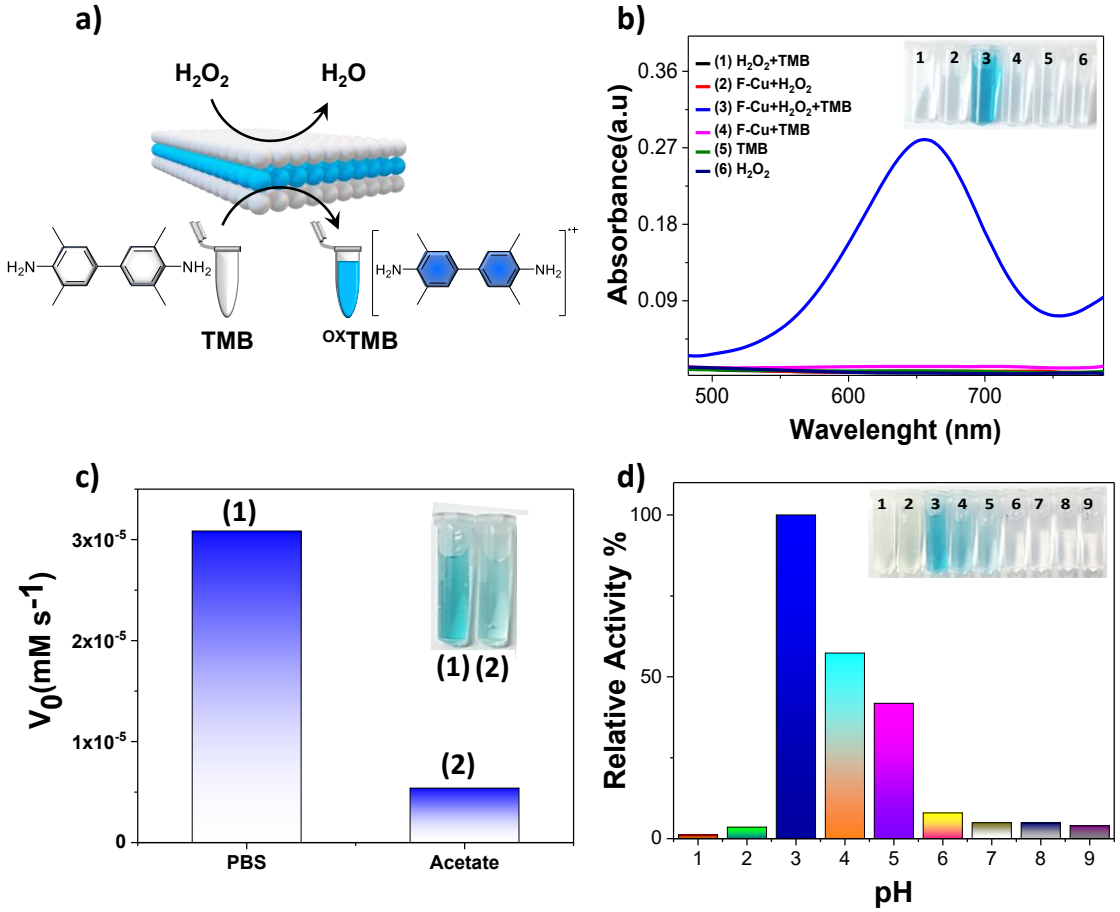

Figure 3. (a) Schematic illustration of POD-mimicking biocatalytic activity of F-Cu bionanozyme. **(b)** UV-visible absorption spectra of substrates in the presence of F-Cu bionanozyme and all the possible control combination studies. **(c)** The kinetics of peroxidase (POD) activity were investigated in both phosphate-buffered saline (PBS) and acetate buffer at pH 3. It was observed that the initial velocity of the reaction in PBS buffer was 5.5 times higher than that in acetate buffer. The inset images distinctly illustrate the development of a more intense blue-colored product in PBS (vial 1) compared to acetate buffer (Vial 2). **(d)** Optimization of POD-like biocatalytic activity of F-Cu on varying ranges of pH [(Acidic (pH-1) to Alkaline (pH-9)].

Next, to confirm the specific role of copper in the F-Cu bionanozyme, we evaluated the peroxidase (POD)-like activity of Phenylalanine (F) conjugated complexes of Zinc (F-Zn)[28], Cobalt (F-Co)[31], and Nickel (F-Ni)[32], synthesized following previously reported methods. Notably, only the copper-containing complex (F-Cu) exhibited significant POD-like activity, while the other metal conjugates showed no detectable activity, as illustrated in **Figure 4a**. This observation highlights the essential role of copper in imparting catalytic functionality to the F-Cu bionanozyme.

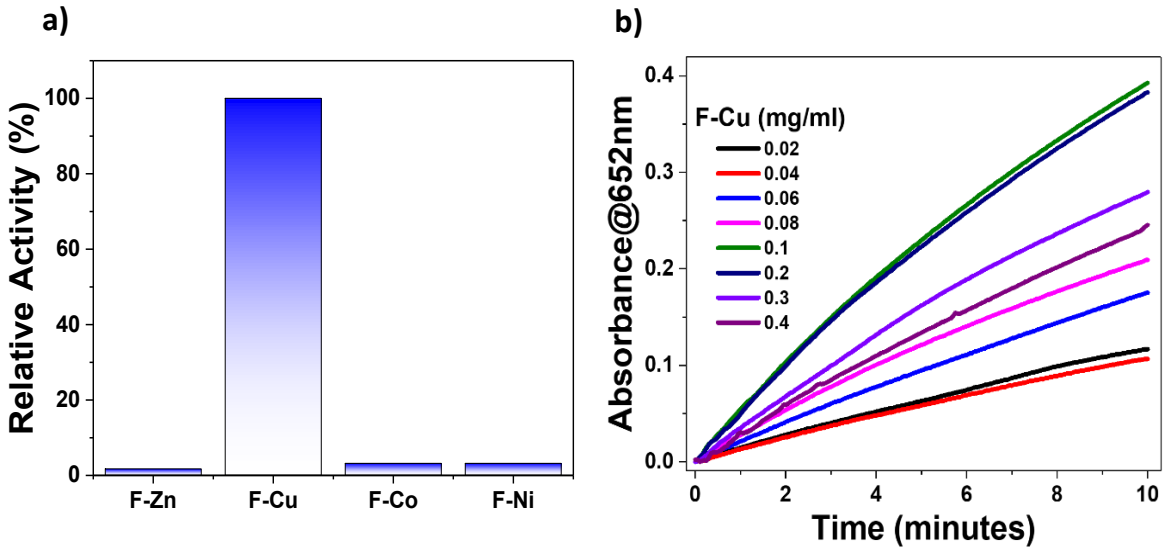

Figure 4. **(a)** Comparison of POD-activity of F-Zn, F-Cu and F-Co and F-Ni, this data shows the POD-activity in case of F-Cu only. **(b)** POD reaction progressed by using varying amounts of F-Cu, and the results demonstrated that the optimum activity of F-Cu was observed at 0.1 mg/mL.

To elucidate the reaction kinetics, the reaction rates were measured under constant optimum catalyst concentration (0.1 mg/mL) (**Figure 4b**) while systematically varying the concentrations of H_2O_2 and TMB. The enzyme-like kinetics of the F-Cu bionanozyme are evident in the relationship between the initial reaction rate and substrate concentration for both H_2O_2 and TMB, as shown in **figure 5a and 5b,** respectively. Initially, an exponential increase in reaction rate is observed, which subsequently plateaus, indicating that further increases in substrate concentration do not significantly impact the reaction rate**.** The initial reaction velocity in relation to substrate concentration aligns well with the Michaelis-Menten (MM) equation, a fundamental model in enzyme kinetics. From the MM fitting analysis, we extracted the maximum reaction rate (V_{max}) and the Michaelis-Menten constant (K_m), which were then compared with literature values **(Figure 5c, d) (Table 1).** For H_2O_2 as the substrate, F-Cu exhibits kinetic parameters with a V_{max} of 1.71×10^{-5} mM/sec, K_m of 0.718 mM and K_{cat} of 3.41/sec Similarly, with TMB as the substrate, the F-Cu bionanozyme demonstrated a V_{max} of 9.3×10^{-5} mM/sec, a K_m of 0.0272 mM and a K_{cat} of 18.5 /s comparable to those reported for the natural enzyme horseradish peroxidase (HRP) ($V_{max} = 10 \times 10^{-5}$ mM/s and $K_m = 0.434$ mM).[16] Notably, the lower K_m values for F-Cu bionanozymes indicate a higher substrate binding affinity compared to HRP enzymes.

Table 1. Comparison of Michaelis Menten parameters with some reported materials.

Material	K_m (mM)		$V_{max} \times 10^{-5}$ (mM/sec)		K_{cat} (Sec^{-1})		Ref.
	TMB	H_2O_2	TMB	H_2O_2	TMB	H_2O_2	
N/S CDs	0.076	0.048	0.309	0.679	-----	-----	[33]
MXene@NiFe-LDH	0.187	0.078	1.707	2.076	-----	-----	[34]
GOx@ZIF-8@Fe-PDA	0.21	0.09	0.74	0.30	-----	-----	[35]
Hemin/ZIF-8	0.024	65.08	0.91	4.20	-----	-----	[36]
$CuFe_2O_4$	2.26	0.50	2.07	2.61	-----	-----	[37]
CDs@ZIF-8-a	0.232	0.737	1.59	1.22	-----	-----	[38]
CDs@Cu-ZIF-8B	0.160	0.232	0.201	0.202	-----	-----	[39]
H_2TCPP-Co_3O_4	0.028	6.10	0.64	0.708	-----	-----	[40]
GO-COOH	0.023	3.99	3.45	3.85	-----	-----	[41]
HRP	0.275	0.214	1.24	2.46	-----	-----	[41]
His-Fe_3O_4	-----	37.99	-----	0.528	-----	-----	[42]
Fe_3O_4	0.382	111	12.3	15.2	3.18×10^{-5}	3.93×10^{-5}	[43]
cofactor-free H15	-----	-----	-----	-----	1.322×10^{-4}	1.147×10^{-4}	[26]
F-Cu	**0.027**	**0.718**	**9.3**	**1.71**	**18.5**	**3.41**	**This work**

Furthermore, to investigate the reaction mechanism involved in the catalytic reduction of H_2O_2 by the F-Cu bionanozyme, we analyzed the fluorescence characteristics of terephthalic acid (TA), a well-established probe in this context. TA, a non-fluorescent compound, undergoes oxidation to form the highly fluorescent O-Hydroxy Terephthalic acid (HTA) in the presence of •OH radicals, rendering it an effective fluorescent probe for detecting •OH radicals. Subsequent to initiating the reaction, TA exhibited a new broad fluorescence emission band centered at 420 nm, indicative of HTA formation **(Figure 6a, b).** This observation confirms the generation of •OH radicals during the F-Cu bionanozyme-catalytic reduction of H_2O_2. While the reaction progressed, the fluorescence emission band at 420 nm steadily increased, signifying a gradual escalation in the •OH intermediate content. This investigation confirms the proficient catalysis of the reduction of H_2O_2 into •OH radicals by the F-Cu bionanozyme, resembling the behavior of the POD enzyme. These radicals subsequently oxidize TA, resulting in the formation of the fluorescent HTA product.

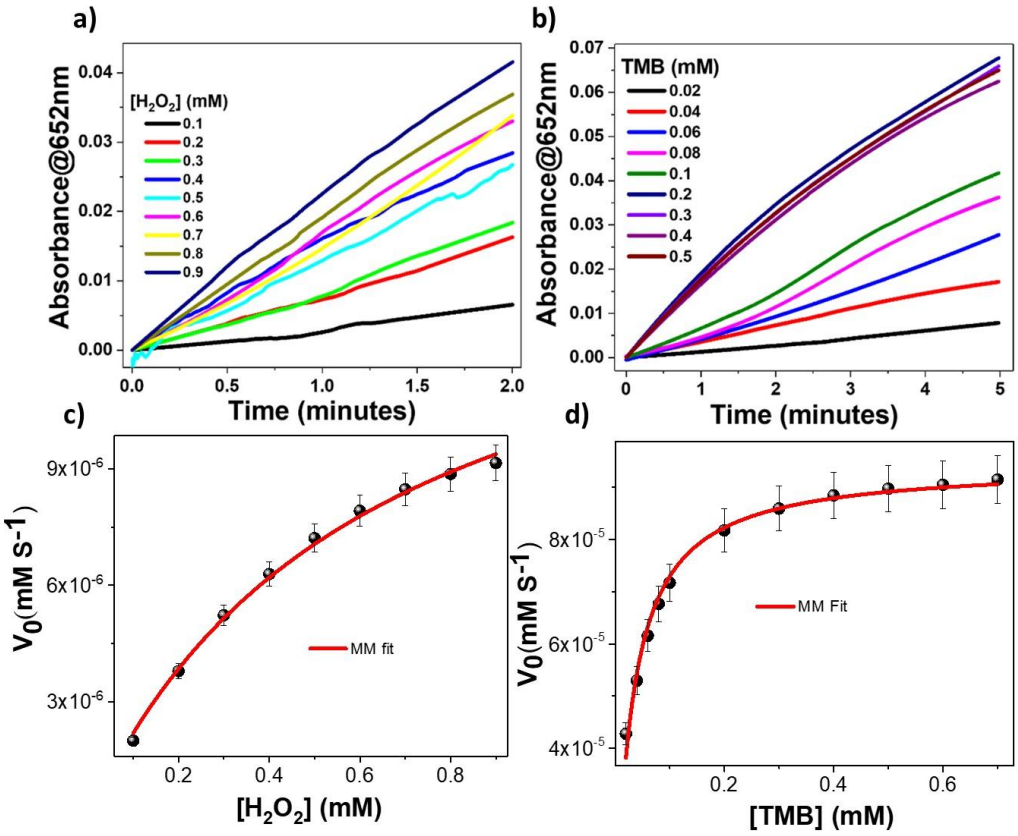

Figure 5. **(a)** Reaction progress with varying ranges of H_2O_2 concentration. **(b)** Reaction progress with varying ranges of TMB concentration at fixed absorbance (652nm) with change of time. **(c, d)** Initial rate (V_0) of the reaction catalysed by F-Cu bionanozyme as a function of substrate [H_2O_2] **(c)** and **(d)** Michaelis-Menten (MM) equation model fitting for H_2O_2 & TMB.

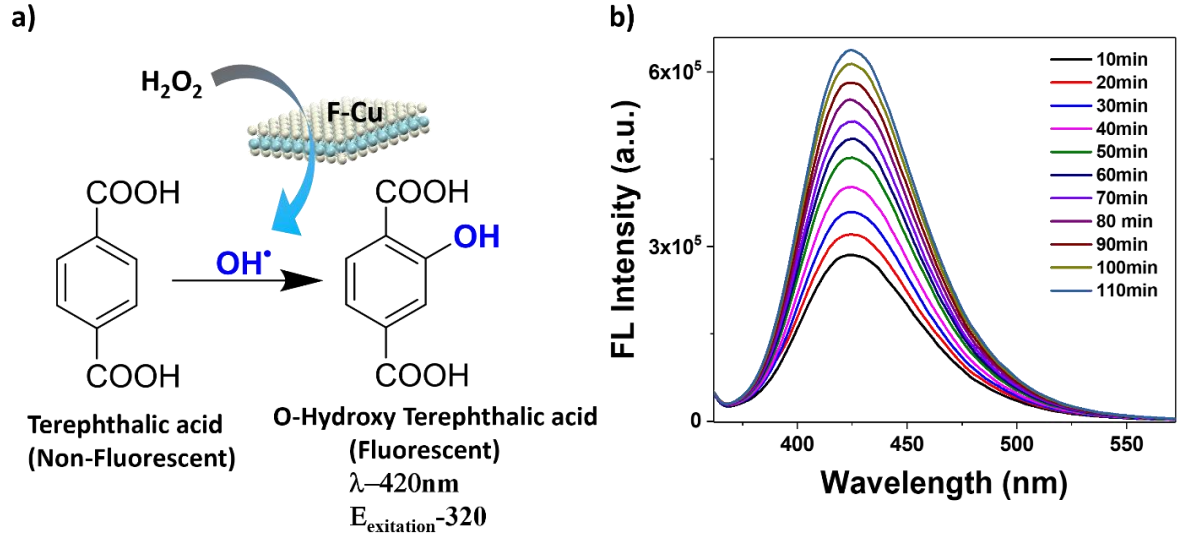

Figure 6. (a) Reaction diagram to show the reaction between terephthalic acid (TA) with hydroxyl radicals (•OH). **(b)** Fluorescent spectra for the in-situ formation of o-hydroxy terephthalic acid (HTA) via TA in the presence of (•OH).

Furthermore, a series of experiments was conducted to gain insights into the reaction intermediates. Notably, reactive oxygen species (ROS) such as superoxide radicals ($O_2^{\bullet-}$) and •OH radicals were selectively scavenged using p-benzoquinone (PBQ) and isopropanol (IPA), respectively by using the previously reported protocol.[44–46] Following the co-incubation of F-Cu, H_2O_2, and TMB with PBQ, IPA, and a combination of both (IPA+PBQ), a substantial reduction in relative activity was observed with IPA+PBQ **(Figure 7a).** In comparison, the samples with IPA and PBQ exhibited approximate declines of 50% and 10%, respectively. These findings suggest that both •OH and $O_2^{\bullet-}$ contribute to the oxidation of TMB, confirming F-Cu bionanozyme Fenton-like catalytic mechanism (Proposed mechanism shown in **Figure 7b).**

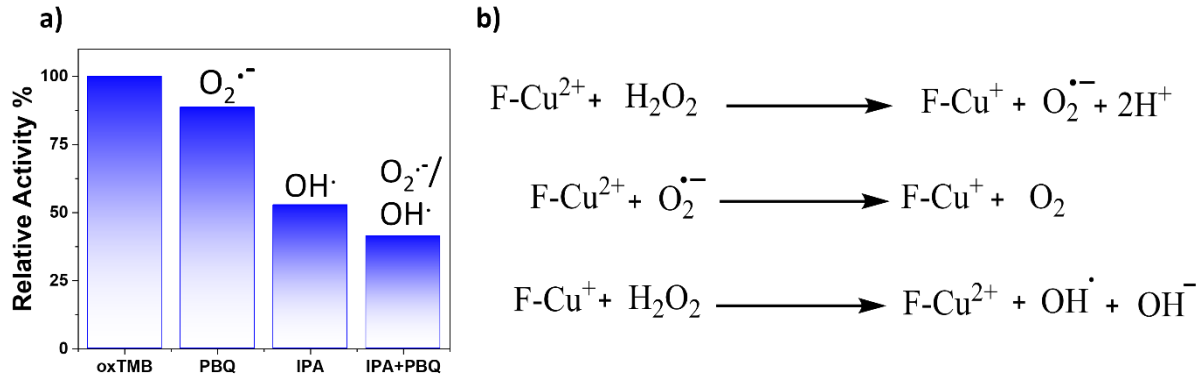

Figure 7. (a) The intensity of the UV−vis absorption of the POD system with various reactive oxygen species (ROS) scavengers like isopropanol for the scavenging of hydroxyl radicals (•OH) and parabenzoquinone for the scavenging of superoxide radical ($O_2^{\bullet-}$). With PBQ the relative activity was observed at 88% while in the case of IPA decreased more up to 52% in the 20-30 seconds. The combined result shows a decrement of 60% due to both (•OH) and ($O_2^{\bullet-}$) ROS species. **(b)** The proposed catalytic reaction mechanism of the F-Cu bionanozyme follows the pathway of a Fenton-like reaction.

Next, POD-like activity of F-Cu have been utilizing to detect H_2O_2, aforementioned that the absorbance of ^{ox}TMB at 652 nm is directly proportional to the concentration of H_2O_2, enabling the quantitative assessment of H_2O_2 based on the catalytic activity of the F-Cu bionanozyme. The absorbance intensity at 652 nm increased progressively with the H_2O_2 concentration, ranging from 0 to 110 µM, as illustrated in **Figure 8a.** This change was also visually apparent, transitioning from colorless to blue, as shown in the inset of **Figure 8a**, providing an immediate visual indication. Within the concentration range of 20 to 110 µM, a linear relationship was observed, allowing the calculation of the limit of detection (LOD) for H_2O_2 to be 5 µM **(Figure 8b**). This LOD is comparable to or surpasses those reported in previous studies **(Table 2).**

These findings highlight the efficacy of the colorimetric detection of H_2O_2 leveraging the POD-mimicking activity of the F-Cu bionanozyme.

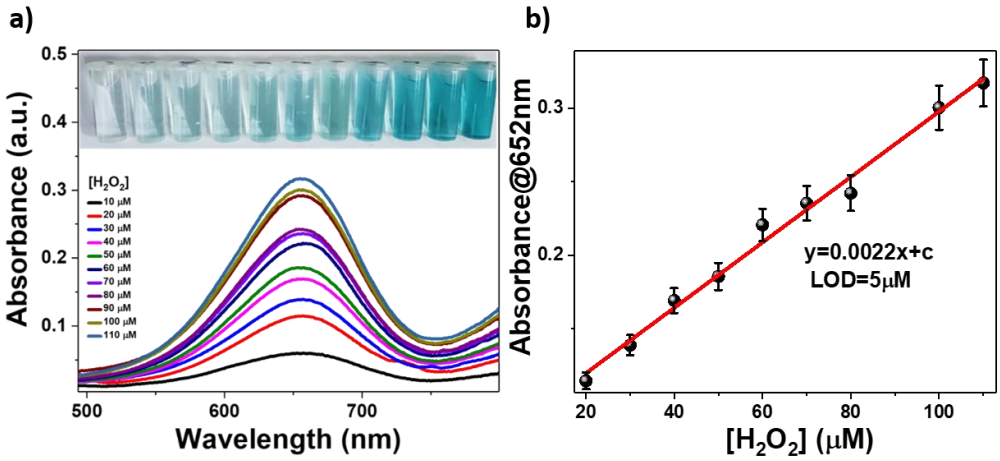

Figure 8. (a) Increase in UV-vis absorbance band on increasing the concentration for the detection of H_2O_2 via F-Cu. **(b)** Standard linear curve for the colorimetric detection of H_2O_2 in a linear concentration range of [H_2O_2] 20-110 µM, with LOD value 5 µM.

Table 2. Comparison of limit of detection linear range for H_2O_2 detection with different materials.

Nanomaterial	Method	LOD (µM)	Linear range (µM)	Ref.
Papain	Colorimetric	2.10	5.00–90.0 µM	47
$CePO_4$: Tb, Gd nanospheres	Colorimetric	5.01	10~500	48
$Cu_2(OH)_3Cl$-CeO_2 nanocomposite	Colorimetric	10	20~50	49
FePt-Au HNPs	Colorimetric	12.33	20–700 µM	50
Au−Ag−Pt Nanoparticle	Colorimetric	54	0-1	51
CoS	Colorimetric	20	50–800	52
GO-FeTPyP	Colorimetric	72	20–500	53
Fe_3O_4@AuNPs	Colorimetric	11.11	40–5500	54
Fe-Ag_2S	Colorimetric	7.82	10–150	55
VB6	Colorimetric	12.10	50–600	56
MnO_2 NWs	Amperometric	10	100–45.4 × 103	57
PET-Ag NWs	Amperometric	46	200–1.5 × 103	58
CoS	Colorimetric	20	50-800	59
NCdots	Colorimetric	15.89	0-500	60
flake-like Cu2O 90.5	Electrochemistry	90.52	0.5–8	61
F-Cu	**Colorimetric**	**5**	**10-140**	**This work**

In practical applications, the stability of a catalyst within industrial settings is of paramount importance. To evaluate the stability of the F-Cu bionanozyme in the catalytic reduction of H_2O_2 under extreme conditions, a series of experiments were conducted. Recyclability was assessed by performing the H_2O_2 catalytic assay, isolating the F-Cu bionanozyme via centrifugation at 12,000 rpm for 10 minutes after each cycle, and rinsing with double-distilled water before reuse. The F-Cu bionanozyme maintained over 94% of its relative catalytic activity after twelve reuse cycles **(Figure 9a)**. The storage stability of the F-Cu bionanozyme was evaluated by incubating it in double-distilled water at 25 °C, with catalytic activity measured every ten days over two months **(Figure 9b)**. The F-Cu bionanozyme retained approximately 97.6% and 96.2% of its relative activity after 30 and 60 days, respectively, demonstrating remarkable storage stability. Thermal stability was first assessed by incubating F-Cu at temperatures ranging from 0 to 110 °C for 40 minutes, followed by conducting a catalytic activity assay at room temperature **(Figure 9c).** Remarkably, the F-Cu bionanozyme demonstrated exceptional thermal stability, maintaining over 95% relative activity across a wide temperature range (20-110 °C). In contrast, the natural enzyme HRP exhibited a gradual decline in activity beyond 30°C due to thermal denaturation, culminating in complete loss of function at approximately 65 °C.[62] Filtration tests further supported these findings by separating the F-Cu bionanozyme from the reaction mixture and conducting the H_2O_2 catalytic assay using the filtrate. The filtrate did not show significant color change, indicating that the catalytic activity is exclusively attributable to the F-Cu bionanozyme **(Figure 9d)**. These rules out the possibility of Cu^{2+} ion release or the involvement of dissolved or non-assembled structures in the filtrate as contributing factors. Next, in situ microscopy was utilized to observe the stability and surface activity ofthe F-Cu bionanozyme during the catalytic H_2O_2 assay, with observations recorded at 15-s intervals over 30 min **(Figure 9e**). Initially, the reaction solution was colorless, along with 2D F-Cu bionanozyme crystals. As the reaction proceeded, the solution developed a pronounced blue hue without altering the underlying 2D morphology of the F- Cu bionanozyme crystals.

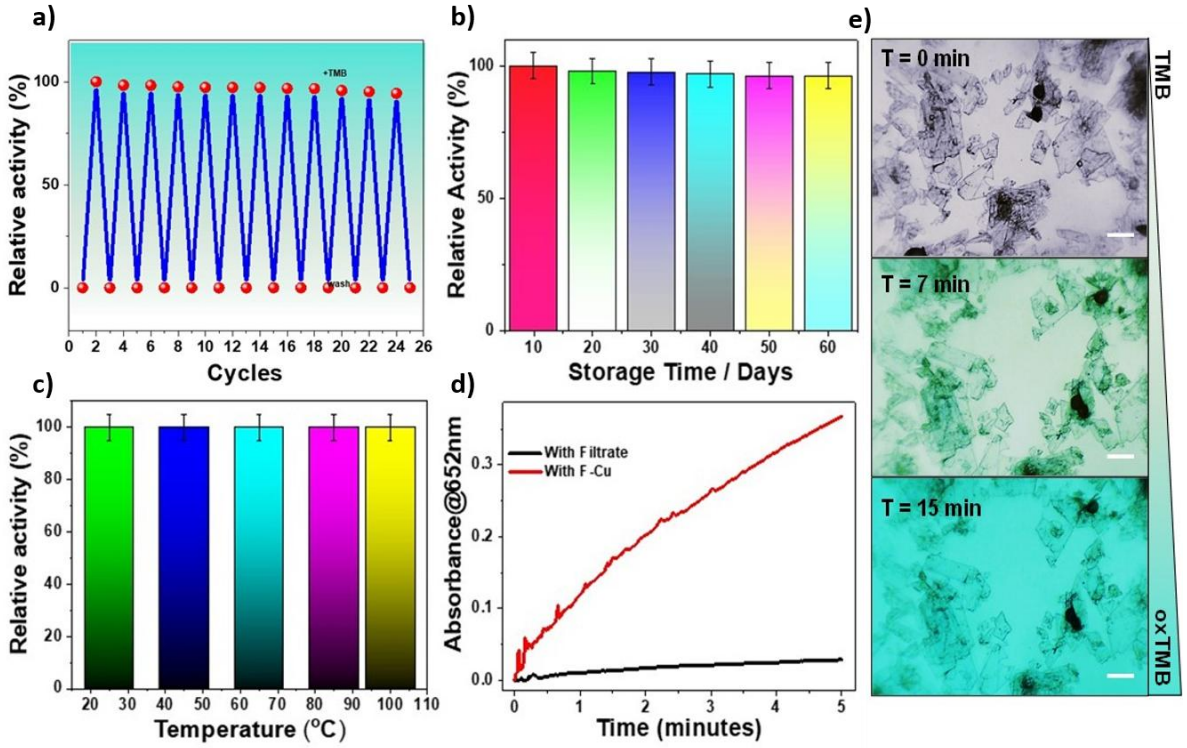

Figure 9. (a) Recyclability of F-Cu up to 12 cycles indicates its high stability during the course of POD activity.. **(b)** Storage stability of F-Cu bionanozymes up to 60 days of time**. (c)** Effect of temperature on the activity POD activity of F-Cu bionanozyme **(d)** Progress of POD reaction by using filtrate of F-Cu which is displayed there is no reaction progress with filtrate against the use of F-Cu as catalysts. **(e)** Optical microscopy snapshots at different intervals (0, 7, and 15 min) taken from the in situ reaction monitoring ofH_2O_2 and TMB catalyzed by F-Cu bionanozyme, the solution color change going from colorless (at 0 min) to blue (after 15 min) indicating the progress of catalytic reaction process.

2.2.3 POD-mimicking F-Cu Bionanozyme Mediated Visual Detection of Dopamine

Having successfully demonstrated the remarkable POD-mimicking capability of the F-Cu bionanozyme, our research focus shifted to exploring its potential for dopamine (DA) detection, as depicted in (Schematics **Figure 10a**). The solution of the F-Cu bionanozyme system (F-Cu+H_2O_2+TMB) displayed a transition from colourless to deep blue, as indicated by the ^{ox}TMB absorption band at 652 nm in the absence of DA. Intriguingly, with the introduction of DA, the intense blue colour diminished, restoring the solution to a colourless state. The photographic evidence and absorption spectra in **Figure 10b**, depicting the impact of varying DA concentrations (ranging from 0 to 200 µM), unveiled a discernible correlation between DA concentration, the fading of the blue-colored solution, and the gradual decline of the corresponding ^{ox}TMB absorption band at 652 nm. This confirmed the DA-induced reduction of ^{ox}TMB to TMB. Furthermore, the calibration curve of absorbance versus DA concentration exhibited linearity within the ranges of 0-80 µM (R2 = 0.99) and 80-200 µM (R^2 = 0.9469), suggesting distinct reaction states of DA **(Figure 10c).** The calculated DA limit of detection (LOD) was as low as 1.5 µM and 9 µM within the respective linear regimes,

indicating the ultra-sensitivity of the POD-mimicking F-Cu bionanozyme system in comparison to prior reports **(refer to Table 3).**

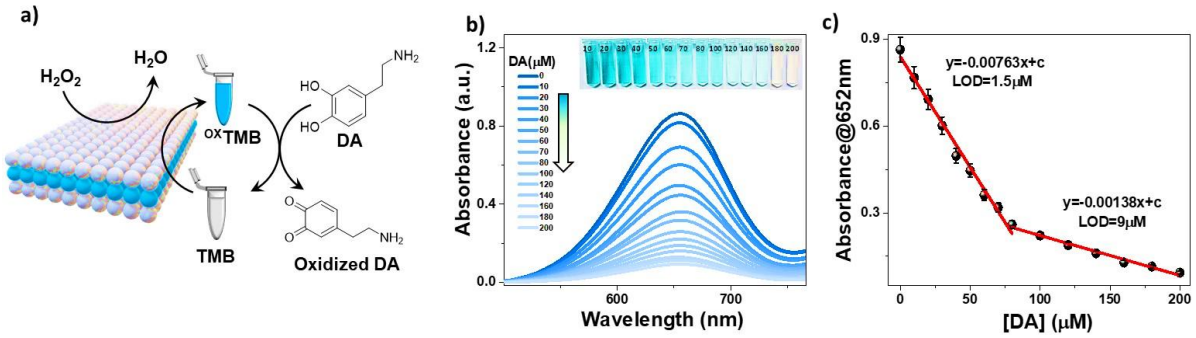

Figure 10. (a) Schematic representation of the DA detection process facilitated by the POD mimicking F-Cu bionanozyme. **(b)** UV-Visible absorption spectra show the change in ^{ox}TMB absorbance with increasing concentrations of DA from 0 to 200 μM. **(c)** The calibration curves for DA concentration range from 0 to 80 μM and from 80 to 200 μM, with the limits of detection (LOD) specified as 1.5 μM for the lower range and 9 μM for the higher range, derived from linear regression analysis.

To assess the DA selectivity of the F-Cu bionanozyme system, interference experiments were conducted in the presence of various analytes including amino acids, metal ions, and a few metabolites. **Figures 11** signify the distinct colour change and relative identification efficiency of DA, suggesting its pronounced impact compared to other substances. This infers that DA selectively reduces the ^{ox}TMB back to TMB. This remarkable selectivity is attributed to dopamine's specific chemical structure, which includes multiple hydrogen atoms on its aromatic ring that enhance electron density and mobility, aiding in the capture of •OH radicals.[80]

Moreover, the practical applicability of the F-Cu bionanozyme system was evaluated through the detection of DA in real samples, including human blood serum, ripped banana peel, and commercially available dopamine hydrochloride injection.[81,82] Using the standard addition method, the concentrations of DA in the aforementioned samples were determined to be 0 μM, 0 μM, and 10 μM, respectively **(Table 4, Figure 12a-c).** Additionally, spiked DA experiments

demonstrated accurate detection in all the real samples with less than 10% error. The combined results indicate that the F-Cu bionanozyme system designed to mimic POD catalytic activity shows promise as an exceptionally sensitive and selective colorimetric DA sensor. This suggests the potential for diverse applications in biomedical diagnostics.

Table 3. Comparison of the limit of detection and linear range for the detection of dopamine (DA) with different materials and methods:

Nanomaterial	Method	LOD (µM)	Linear range (µM)	Ref.
Co_3O_4@NiO	Colorimetric	1.21	1–1000	63
Ag NPs	Colorimetric	1.20	3.20–20	64
Fe_3O_4 NPs	Colorimetric	3.50	0.010-4.0	65
CQDs/CuO	SWV	2.54	1-180	66
Au-Cu_2O/rGO/GC	DPV	3.90	10-90	67
Nanostructured Gold	DPV	5.00	10-100	68
CuS Nanocubes	Colorimetric	1.67	2-150	69
CA-Cu	Colorimetric	2.23	-------	70
Au NPs	Colorimetric	2.50	2.5-20	71
Nanoceria	Colorimetric	1.50	1-800	72
CAuNE	Electrochemical	5.83	1–100	73
Calcein blue-Fe^{+2}	Fluorescence	10	50-1000	74
3D-rGO/Fe3O4/HP-β-CD/GCE	Electrochemical	5	0.02-25	75
AgNPs/rGO)	Electrochemical	5.41	10–800	76
Chitosan-CNT	Electrochemical	2.52	0-10	77
Gr	Electrochemical	2.64	4-100	78
Gr-AuNPs	Electrochemical	1.86	5-1000	79
F-Cu	**Colorimetric**	**1.51**	**0-80**	**This work**

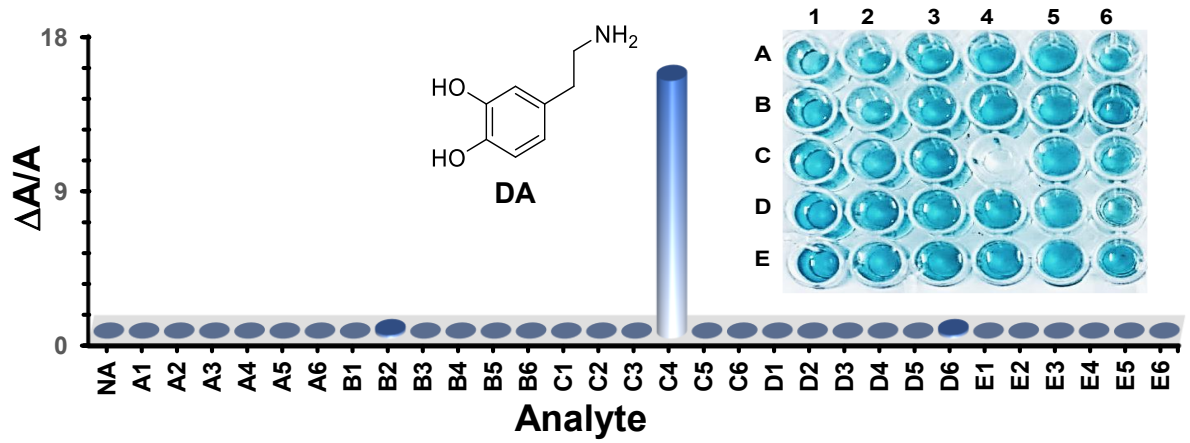

Figure 11. Inset photograph of a microwell plate with various analytes reacting in a mixture of F-Cu, H_2O_2, and TMB, highlights the equipment-free visual detection capability for DA (specifically in well C4), as indicated by the color change from blue to colorless (A1 = L-Phenylalanine, A2 = L-Lysine, A3 = L-Histidine, A4 = L-Proline, A5 = L-Serine, A6 = L-Tryptophan, B1 = L-Tyrosine, B2 = L-Cysteine, B3 = L-Glutamic acid, B4 = L-Arginine, B5 = L-Aspartic acid, B6 = Glycine, C1 = L-Alanine, C2 = L-Valine, C3 = L-Isoleucine, C4 = DA, C5 = L-Methionine, C6 = D-Glucose, D1 = L-Leucine, D2 = L-Threonine, D3 = L-Asparagine, D4 = Uric Acid, D5 = L-Glutamine, D6 = Ascorbic acid, E1 = Mn^{2+}, E2 = Co^{2+}, E3 = Zn^{2+}, E4 = K^{+}, E5 = Na^{+}, E6 = Cu^{2+}). Each interfering analyte was tested at a concentration of 200 µM. The corresponding net absorbance change (ΔA/A) at 652 nm for each analyte, underscores the selective response towards DA (well C4).

Moreover, the practical applicability of the F-Cu bionanozyme system was evaluated through the detection of DA in real samples, including human blood serum, ripped banana peel, and commercially available dopamine hydrochloride injection.[81,82] Using the standard addition method, the concentrations of DA in the aforementioned samples were determined to be 0 µM, 0 µM, and 10 µM, respectively **(Table 4, Figure 12a-c).** Additionally, spiked DA experiments demonstrated accurate detection in all the real samples with less than 10% error. The combined results indicate that the F-Cu bionanozyme system designed to mimic POD catalytic activity shows promise as an exceptionally sensitive and selective colorimetric DA sensor. This suggests the potential for diverse applications in biomedical diagnostics.

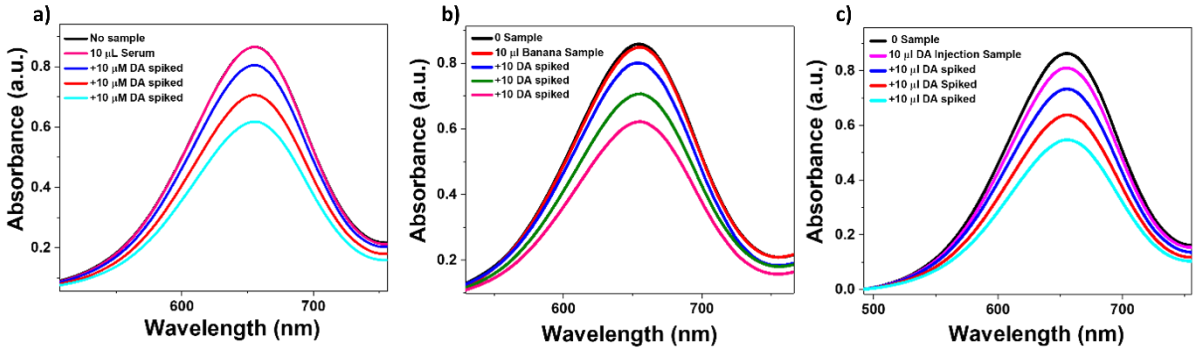

Figure 12. Response of ^{ox}TMB UV-visible band on adding real samples for the detection of DA. **(a)** Human blood serum. **(b)** Ripped banana peel. **(c)** Commercially available dopamine hydrochloride injection.

Table 4. F-Cu bionanozymes mediated DA detection from real sample extracts.

Sample	Spiked [DA] (μM)	Total [DA] spiked (μM)	Detected [DA] (μM)	% Error
Blood Serum	0	0	0	NA
	10	10	9.95	0.5
	10	20	20.21	1.05
	10	30	29.74	0.86
Ripped Banana Peel	0	0	0	NA
	10	10	10.21	2.10
	10	20	20.18	0.90
	10	30	30.14	0.46
Dopamine Injection	0	0	10	NA
	10	10	20.08	0.40
	10	20	30.67	2.23
	10	30	40.61	1.52

2.2.4 POD-mimicking F-Cu Bionanozyme Mediated Visual Detection of nitrite (NO_2^-)

Interestingly, it was observed that the addition of nitrite (NO_2^-) altered the colour of the F-Cu bionanozyme system (F-Cu+H_2O_2+TMB) solution. As shown in **figure 13a**, the F-Cu bionanozyme system initially exhibits a blue colour due to the POD mimicking catalytic oxidation of TMB. Upon the addition of a small amount of NO_2^- (100 μM), the solution's colour transitions from blue to yellow. Correspondingly, the UV-vis absorption signal at 652 nm, attributed to ^{ox}TMB, decreases in the presence of NO_2^-, while a new significant signal appears at approximately 445 nm **(Figure 13b)**. This phenomenon can be attributed to the reaction between ^{ox}TMB and NO_2^-. The aromatic primary amine group in ^{ox}TMB reacts with NO_2^- in an acidic environment (pH 4) to undergo a typical diazotization reaction.[7] Consequently, the consumption of blue ^{ox}TMB reduces the original signal at 652 nm and the formation of yellow colored product is the colorimetric signal for the nitrite ion detection Next, **figure 13c** demonstrates the impact of varying concentrations of NO_2^- (0-140 μM). Furthermore, the calibration curve of absorbance versus NO_2^- concentration exhibited linearity within the range of 0-60 μM ($R^2 = 0.99$) **(Figure 13d)**. The calculated limit of detection (LOD) for NO_2^- was as low as 4 μM, indicating the ultra-sensitivity of the F-Cu bionanozyme system compared to prior reports **(refer to Table 5).** Crucially, the cascade of POD-mimicking catalysis and diazotization demonstrates high specificity toward nitrite. **Figure 13e** compares the responses of various interfering analytes, including amino acids, metal ions, and certain metabolites, to the F-Cu bionanozyme system. The results indicate that only NO_2^- triggers the generation of the signal at 445 nm, highlighting the system's excellent selectivity toward the target analyte. This specificity forms the basis for NO_2^- detection. To evaluate the feasibility of the F-Cu bionanozyme system for detecting NO_2^- in real samples, we analyzed NO_2^- in commonly consumed green vegetables such as carrots and spinach.[8] A well-established procedure was

employed to extract nitrite ions from carrots and spinach, and the detection assay was conducted.[7,83] Interestingly, NO_2^- was detected in carrot and spinach extracts at approximately 0 µM and 0 µM, respectively **(Figure 14a-b, Table 6).** Moreover, spiked experiments demonstrated less than 7% error in detecting NO_2^- ions in real samples, suggesting the system's practical applicability. Hence, the F-Cu bionanozyme system for catalytic detection of NO_2^- is anticipated to have potential applications in food safety monitoring and other relevant fields.

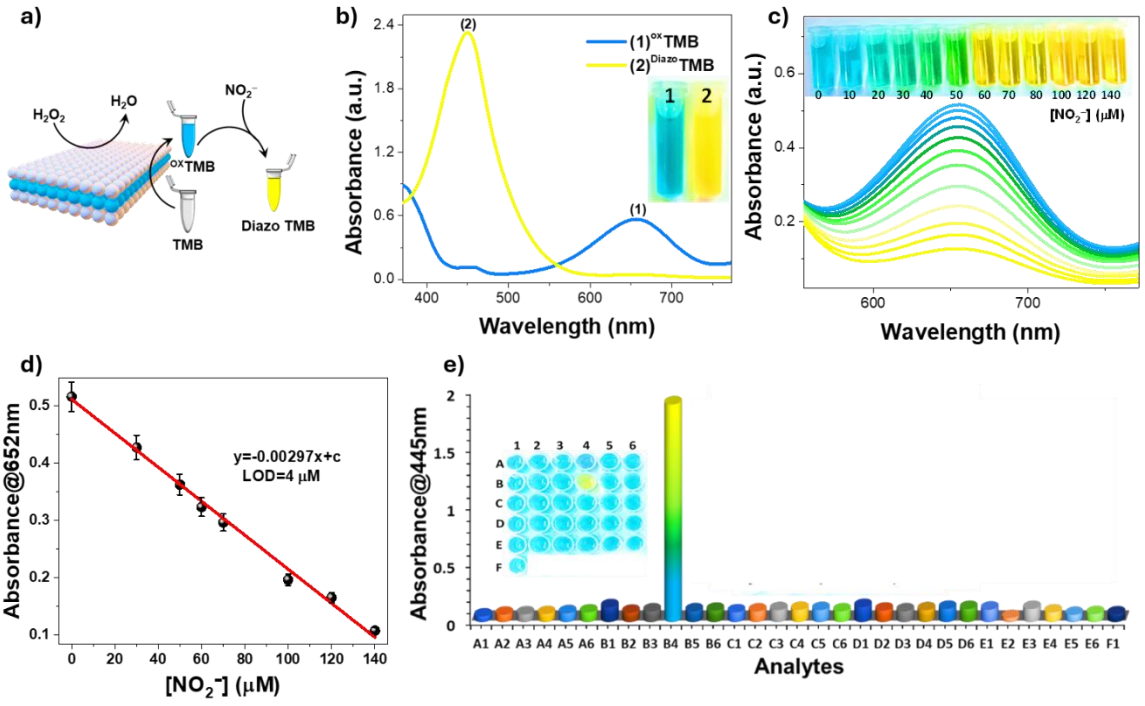

Figure 13. (a) Schematic representation of the mechanism for NO_2^- detection mediated by F-Cu bionanozymes. **(b)** UV-visible absorption spectra show the transformation of oxTMB to ^{Diazo}TMB in the presence of NO_2^-, highlighted by the emergence of a new absorption band at 445 nm. **(c)** UV-visible spectra demonstrating the effect of increasing concentrations of NO_2^- (ranging from 0 to 140 µM) on oxTMB. **(d)** Calibration curve depicting the linear response of NO_2^- ion concentration (0-140 µM) at an absorbance of 652 nm, with a calculated limit of detection (LOD) of 4 µM based on linear regression analysis. **(e)** Comparative analysis of absorbance changes at 445 nm in the presence of various interfering analytes (A1 = L-Phenylalanine, A2 = L-Lysine, A3 = L-Histidine, A4 = L-Proline, A5 = L-Serine, A6 = L-Tryptophan, B1 = L-Tyrosine, B2 = L-Cysteine, B3 = L-Glutamic acid, B4 = NO_2^-, B5 = L-Aspartic acid, B6 = Glycine, C1 = L-Alanine, C2 = L-Valine, C3 = L-Isoleucine, C4 = DA, C5 = L-Methionine, C6 = D-Glucose, D1 = L-Leucine, D2 = L-Threonine, D3 = L-Asparagine, D4 = L-Glutamine, D5 = Mn^{2+}, D6 = Co^{2+}, E1 = Zn^{2+}, E2 = K^+, E3 = Na^+, E4 = Cu^{2+}, E5=NO_3^-, E6=SO_4^{2-}, F1=PO_4^{3-}), showcasing the exceptional selectivity of the assay towards NO_2^- (B4). Each interfering analyte was tested at a concentration of 140 µM. Inset: A photograph of a microwell plate illustrating the assay's capability for equipment-free, visually distinct detection of NO_2^-, as evidenced by a selective color change to yellow in well B4.

Table 5. Comparison of the limit of detection and linear range for the detection of nitrite (NO_2^-) with different materials and methods.

Nanomaterial	Method	LOD (µM)	Linear range (µM)	Ref.
AuNP–CeO_2 NP@GO	Colorimetric	4.61	100-5000	84
PEG hydrogel	Colorimetric	10	10-5000	85
Cu-MOF	Colorimetric	8.53	12-300	86
1-NAP	Colorimetric	10	10-500	85
AgZEGE	Electrochemical	10	100-1000	87
Nanometer-sized gold Colloid	Electrochemical	45	130-44,000	88
ND powder electrode	Electrochemical	120	100-12,000	89
ccNIR/GCE	Electrochmical	5.45	5.4-43.4	90
GCE/f-ZnO@rFGO	Electrochmical	33	10-500	91
Hb/Ag nanoparticles/TiO2	Electrochmical	34	200-600	92
F-Cu	**Colorimetric**	**4**	**0-140**	**This work**

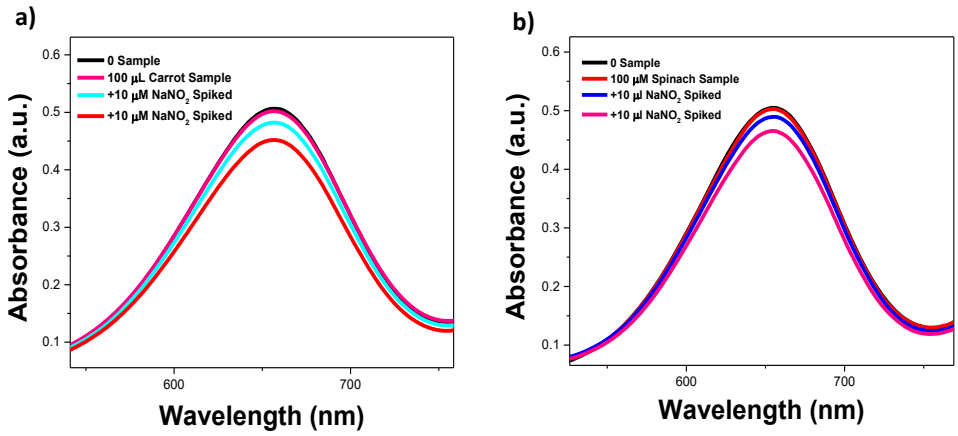

Figure 14. Response of ^{ox}TMB UV-visible band on adding real samples for the detection of nitrite **(a)** Carrot extract. **(b)** Spinach extract.

Table 6. F-Cu bionanozymes mediated NO_2^- detection from real sample extracts.

Sample	Spiked [NO_2^-] (μM)	Total [NO_2^-] (μM)	Detected [NO_2^-] (μM)	% Error
Carrot	0	0	0	NA
	10	10	10.21	2.10
	10	20	21.05	5.25
Spinach	0	0	0	NA
	10	10	9.5	5.00
	10	20	21.4	7.00

2.2.5 Sequential Detection of Analytes using F-Cu Bionanozyme-Based Logic Gate Systems

This study describes a unique approach for the sequential detection of analytes employing a logic gate-inspired F-Cu bionanozyme system **(Figure 15).** By leveraging the colorimetric properties of chromogenic substrates, this system enables visually identifiable and sequential detection of target molecules through distinct color changes. The methodology mimics the operation of logic gates, where specific combinations of inputs result in predefined outputs. Here, analytes are designated as input signals (e.g., Input A and Input B), and the colorimetric responses represent output signals (e.g., Output Z). Logic Gate Design for H_2O_2 and DA Detection **(Figure 15a and 15b)**: The system employs F-Cu bionanozyme to detect hydrogen peroxide (H_2O_2, Input A) and dopamine (DA, Input B). In this process, Input A (H_2O_2) triggers a reaction between the F-Cu bionanozyme and TMB substrate, producing a blue-colored product (^{ox}TMB). This signifies Output Z = 1, visually indicating the presence of H_2O_2. Input B (DA), when introduced after H_2O_2, reduces oxTMB to its colorless form, effectively turning Output Z = 0. This output change signifies the presence of DA. The corresponding truth table **(Figure 15b)** reflects the NOT-NOR logic gate functionality (NOT Gate: Inverts the input signal; NOR Gate: Outputs 1 only when both inputs are 0), where the initial output Z = 1 confirms H_2O_2 detection, and the transition to Z = 0 upon DA introduction indicates its presence. The absence of either analyte results in no color change (Z = 0), completing the NOT-NOR gate operation. Logic Gate Design for H_2O_2 and NO_2^- Detection **(Figure 15c and 15d)**: Another implementation of the F-Cu bionanozyme logic gate involves the sequential detection of hydrogen peroxide (H_2O_2, Input A) and nitrite ions (NO_2^-, Input B). In this system, Input A (H_2O_2) reacts with the F-Cu bionanozyme and TMB, forming oxTMB and producing a blue color (Output Z = 1). Input B (NO_2^-), introduced subsequently, reacts with ^{ox}TMB to form ^{diazo}TMB, leading to a yellow-colored product. The system retains Output Z = 1, indicating successful detection of both analytes. The truth table **(Figure 15d)** illustrates this AND-OR logic gate behavior (AND Gate: Outputs 1 only when both inputs are 1; OR Gate: Outputs 1

when at least one input is 1). The blue-to-yellow color change upon sequential introduction of NO_2^- validates its detection while confirming the presence of H_2O_2.

This logic gate-inspired colorimetric system offers several advantages, including simplicity, cost-effectiveness, and visual interpretability. Its potential applications span environmental monitoring, healthcare diagnostics, and food safety, where rapid and sequential analyte detection is critical. The user-friendly nature of this technique, coupled with the tunable properties of bionanozyme-based sensors, underscores its versatility in biosensing platform development.

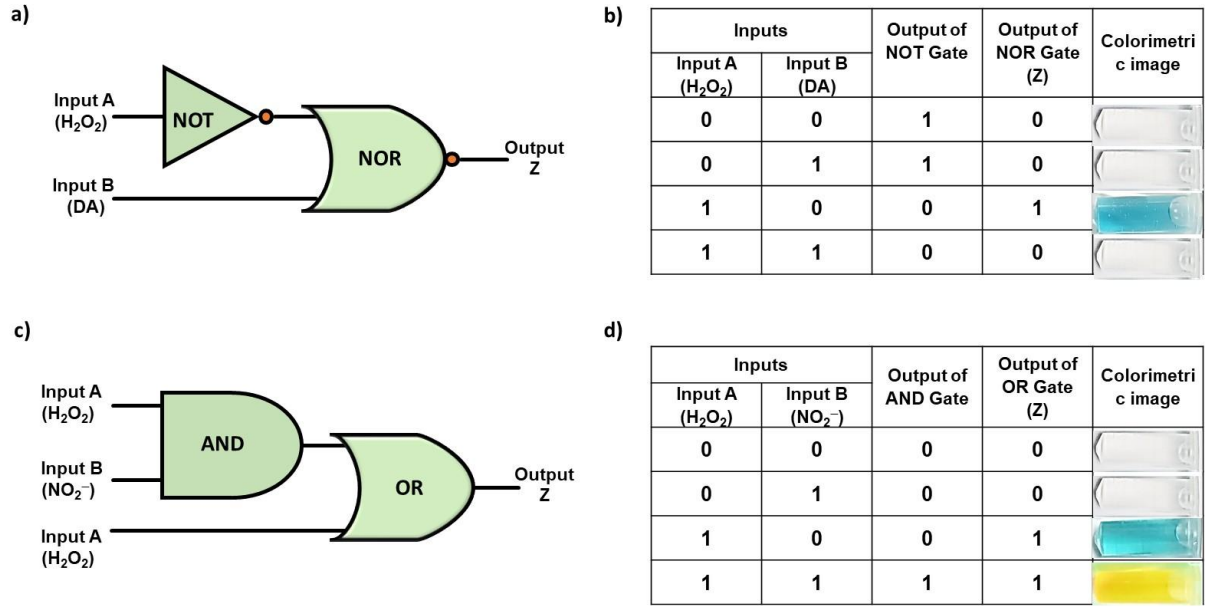

Inputs		Output of NOT Gate	Output of NOR Gate (Z)	Colorimetric image
Input A (H_2O_2)	Input B (DA)			
0	0	1	0	
0	1	1	0	
1	0	0	1	
1	1	0	0	

Inputs		Output of AND Gate	Output of OR Gate (Z)	Colorimetric image
Input A (H_2O_2)	Input B (NO_2^-)			
0	0	0	0	
0	1	0	0	
1	0	0	1	
1	1	1	1	

Figure 15. Logic gate **(a and c)** and truth table **(b and d)** of the F-Cu bionanozyme system for the consecutive detection of H_2O_2 and DA **(a and b)** as well as H_2O_2 and NO_2^- **(c and d).**

2.3 Conclusions

In summary, we have successfully developed the simplest POD-mimicking single amino acid F-Cu bionanozyme system as an ultrasensitive colorimetric probe for detecting crucial biomarkers such as H_2O_2, dopamine, and nitrite ions. By leveraging the unique properties of F coordinated with Cu^{2+} ions, we synthesized F-Cu bionanozymes with a two-dimensional hierarchical structure, featuring a dense arrangement of crystalline orderly redox-active (Cu^{2+}/Cu^{+}) accessible catalytic sites. The F-Cu bionanozyme demonstrates remarkable POD-like catalytic activity, capable of rapidly reducing H_2O_2 through a Fenton-like reaction mechanism while maintaining robustness under extreme pH variations, long-term storage, and elevated temperatures. Its ultrasensitive and rapid detection capabilities have been validated

with detection limits as low as 5 μM for H_2O_2, 1.5 μM for DA, and 4 μM for nitrite ions. These outstanding performance characteristics align with the WHO-REASSURED criteria, making this bionanozyme a potential candidate for biosensing applications in resource-limited settings. These findings underscore the potential of bioinspired de *novo-designed* bionanozymes in overcoming the drawbacks associated with natural enzymes, including production costs, stability, and reusability. The minimalistic approach of utilizing a single amino acid and Cu^{2+} ions not only simplifies the synthesis process but also enhances the functional versatility and stability of the resulting bionanozyme. The implications of this research extend beyond immediate biosensing applications, laying the groundwork for the rational design of more sophisticated artificial enzymes. Our future endeavors will focus on the further refinement of bionanozyme design, the expansion of its range of applications, and its integration into practical diagnostic and monitoring devices. This initiative holds significant promise for a wide spectrum of applications in point-of-care diagnostics, biotechnology, environmental monitoring, food safety, and healthcare.

2.4. Experimental Section:

1. Materials and Methods

L-Phenylalanine, Copper chloride dihydrate, Hydrogen peroxide, 3,3',5,5'-tetramethylbenzidine (TMB), Dimethyl sulfoxide (DMSO), Dopamine hydrochloride, Glutathione, L-Leucine, L-Lysine, L-Methionine, L-Histidine, D-Glucose, L-Proline, Dopamine, L-Serine, L-Threonine, L-Tryptophan, L-Asparagine, L-Tyrosine, Uric acid, L-Cysteine, L-Glutamine, L-Glutamic acid, Ascorbic acid, L-Arginine, L-Aspartic acid, Glycine, L-Alanine, L-Valine, L-Isoleucine, Manganese chloride, Cobalt chloride, Zinc chloride, Sodium chloride, Potassium chloride, and Terephthalic acid were purchased from Sigma-Aldrich. All materials were used as received. Double distilled (DD) water was used to prepare all the buffers and solutions.

2. Synthesis of F-Cu Bio-nanozyme

Under heating (60 °C) condition, an aqueous solution of one equivalent of the $CuCl_2$ (85.24mg, 10 mM) was slowly added to two equivalents of an alkaline solution of L-Phenylalanine (F) (82.50mg, 10 mM) containing (20mg, 10 mM) of NaOH solution total volume of the mixture was 50 mL. After 10-15 minutes 2D-plate-like crystals started to form. After 30 minutes, the reaction mixture was cooled down to room temperature. The formed crystals were collected by filtration and washed with double-distilled water and ethanol to eliminate any unreacted reactants.

3. Characterizations Techniques Used in This Study

3.1. Optical Microscopy: The Olympus C43 microscope was used to snap pictures of 2D crystals of F-Cu and to record videos of catalysis as shown.

3.2. High-Resolution Scanning Electron Microscopy (HR-SEM): F-Cu samples were coated with Cr after being placed on a clean microscope glass coverslip. The images were snapped with a JSM-6700 field emission scanning electron microscope (JEOL, Tokyo, Japan) with the voltage set to 10 kV.

3.3. Atomic Force Microscopy (AFM): The F-Cu crystals were placed onto a clean microscope glass coverslip before and after a 10-minute ultrasonication treatment. The samples were characterized using the non-contact (tapping) mode of the AIST-NT Smart AFM instrument, Cantilevers of silicon nitride 100 mm long (OMCL- RC800PSA-W, Olympus) having a resonance frequency of 70 kHz. WSxM imaging software was used to analyse and show the pictures.

3.4. UV-vis Spectrophotometer: The complexation between Cu^{2+} and F and all catalysis were studied using a UV-visible spectrophotometer (An Agilent Cary-60).

3.5. Powder X-ray Diffraction (PXRD): The F-Cu nanosheets were applied onto a quartz sample holder with no background interference. Powder X-ray diffraction (XRD) analysis was conducted on a Bruker D8 Advance X-ray powder diffractometer at room temperature, with measurements taken within the 5 to 45° 2θ range. The backdrop was removed to isolate the diffraction peaks.

3.6. X-ray Photoelectron Spectroscopy (XPS): To confirm the elemental compositions and oxidation state of Cu metal in F-Cu, XPS spectra were collected by using XPS K-Alpha (Thermo Fisher Scientific). F-Cu samples were coated on a clean microscope glass coverslip and made dry to collect the XPS data.

4. POD Mimicking Catalytic Activity of F-Cu Bionanozyme: The POD-like activity of the F-Cu bio-nanozyme was examined using an optimum concentration of H_2O_2 and TMB as substrates. 0.2 mM of TMB (stock solution: 20 mM in DMSO) and 0.9 mM H_2O_2 (Stock solution: 50 mM) were in PBS (1X) buffer of pH-3.0 and the final volume was made 2mL **(Refer Figure 4b, Figure 5a,b,** for F-Cu, H_2O_2 and TMB optimizations). Then, 200 µL of the F-Cu suspension (1 mg/mL in DMSO) was added to the assay. After 5 min of incubation, the absorption spectrum of the reaction mixture was recorded.

4.1. Steady-State Kinetics Study: In order to optimize the performance of the F-Cu bionanozyme for H_2O_2 catalysis, a series of experiments were conducted to determine the optimal experimental parameters, including pH, substrate concentration, and response time. **Figure 3d** illustrates that the highest catalytic activity of the F-Cu bionanozyme was observed at pH 3. Therefore, pH 3 was selected as the optimal condition for subsequent experiments. Additionally, based on the results in **Figure 4b,** the optimal F-Cu concentration was determined to be 0.1 mg mL^{-1} after evaluating a range of concentrations from 0.02 to 0.4 mg mL^{-1}. Temperature effects were assessed within the range of 25 °C to 100 °C **(Figure 9a)**, revealing that the maximum catalytic activity occurred at 25 °C. Consequently, 25 °C was set as the optimal reaction temperature. The optimal absorbance was attained within a 3-minute timeframe, identifying this duration as the optimal reaction time. Under these optimized conditions (pH 3.0, 25 °C, 3 minutes, and a catalyst concentration of 0.1 mg mL^{-1}), the F-Cu bionanozyme exhibited the highest peroxidase-mimicking activity in the colorimetric catalytic system. In addition, concentration-dependent investigations were carried out for H_2O_2 (0.1-0.9 mM) and TMB (0.02-0.5 mM) **(Figure 5a and 5b).** The results showed that the most significant activity was observed at 0.9 mM of H_2O_2 and 0.2 mM of TMB. Therefore, the optimized conditions were set at 0.9 mM of H_2O_2 and 0.2 mM of TMB. All these optimized conditions F-Cu (0.1 mg mL^{-1}) + TMB (0.2 mM) + H_2O_2 (0.9 mM) in PBS (pH 3) at 25 °C, 3

min incubation time) were subsequently applied to both dopamine and nitrite ion detection assays.

4.2. Mechanism of POD-like Activity of F-Cu Bio-nanozyme:

To characterize the hydroxyl radicals (•OH) intermediates generation during the F-Cu catalytic TMB oxidation, we carried out a Terephthalic acid (TA) assay.[93] 200 µL of TA (3 mM, 15 mg/30 mL water) and 200 µL of F-Cu (stock solution 1 mg/mL, water) were added into 1.6 mL PBS (1X, pH-3) solution. The fluorescence emission signal for O-Hydroxy Terephthalic acid (HTA) was observed at around 420 nm with an excitation wavelength of 320 nm. Further, the reaction mixtures at different time intervals (10, 20, 30, 40, 50, 60, 70, 80, 90, 100, and 110 minutes) were analysed by fluorescence spectrophotometer. The time-dependent increase in fluorescence intensity at 425 nm suggests the time-dependent (•OH) radical generation for the conversion of nonfluorescent TA into fluorescent HTA. Overall, this experiment confirms the F-Cu catalytic conversion of H_2O_2 into (•OH) radicals.

4.3. Colorimetric Detection of H_2O_2: The F-Cu bionanozymes H_2O_2 detection capability was evaluated within a concentration range of 10-110 µM. The assay was conducted in a pre-optimized PBS buffer solution maintained at pH 3.0 for optimal activity **(Figure 3d)**. Experimental conditions mirrored previously described protocols, employing 0.1 mM of the chromogenic substrate, 3,3',5,5'-tetramethylbenzidine (TMB), and 0.1 mg/mL of the F-Cu bionanozyme.

Varying H_2O_2 concentrations were introduced by adding aliquots of H_2O_2 solution to a reaction mixture containing TMB and F-Cu in PBS buffer. This mixture underwent incubation for 2-3 minutes at room temperature. This incubation period was chosen based on the established kinetic profile **(Figure 5a)** to ensure sufficient reaction time while minimizing potential interferences from side reactions. During incubation, the H_2O_2, TMB, and F-Cu interact, leading to the formation of a colored complex detectable by UV-visible spectroscopy.

Following incubation, the UV-visible absorption spectra of each sample were acquired. As expected, a direct correlation between H_2O_2 concentration and absorbance was observed **(Figure 8a)**. Higher H_2O_2 concentrations resulted in increased absorbance values. The peak absorbance at 652 nm was then plotted against the corresponding H_2O_2 concentrations to generate a calibration curve **(Figure 8b)**. This calibration curve was utilized to determine the limit of detection (LOD), which represents the smallest reliably detectable H_2O_2 concentration based on observed changes in absorbance. In this instance, the LOD was determined to be 5 µM within the tested concentration range of 10-110 µM.

Limit of detection (LOD) = 3s/m

Where, s = Standard deviation; m = slope

5. Colorimetric Detection of Dopamine (DA):

Optimized conditions for the POD-like activity of F-Cu (Described in section 4) were utilized for the colorimetric detection of DA. For this purpose, different concentrations of dopamine (0, 10, 20, 30, 40, 50, 60, 70, 80, 100, 120, 140, 180, 200 μM) were added to the POD system. The time interval was carefully maintained at 25°C for each example. Next, each sample was employed to record UV-vis spectra by using 3.5 mL of quartz cuvette. Next, a plot was constructed between absorbance at 653 nm vs [DA] concentration in μM. There are two linear slopes obtained: one in the concentration range of 0-80 μM and another 80-200 μM respectively. Next, LOD was calculated corresponding to both concentration ranges are 1.5 and 9 μM respectively.

5.1 Interference Experiment for DA Detection: Interference experiment has been conducted to demonstrate the sensitivity of this approach. In this experiment, we introduced a concentration of 200 μM for each analyte into the peroxidase (POD) system, as outlined in section 4. This particular 200 μM concentration is crucial because it represents the point at which dopamine (DA) completely reduced oxidized TMB (^{ox}TMB). Along with 200 μM of each analyte, 0.2 mM TMB (prepared from a 20 mM stock solution in DMSO), and 0.9 mM hydrogen peroxide (H_2O_2) (from a 50 mM stock solution) were all mixed in phosphate-buffered saline (PBS, 1X) at pH 3.0. Additionally, 200 μL of the F-Cu suspension (1 mg/mL in DMSO) was added to the reaction mixture. The total volume of each reaction was adjusted to 2 mL. After adding each analyte to the system, the samples were incubated for 2 minutes. This incubation period was determined to be the minimum time necessary to observe a significant color change and a corresponding change in the absorbance of ^{ox}TMB to TMB. Notably, among all the analytes tested, only dopamine (DA) exhibited a response by reducing ^{ox}TMB, as illustrated in **Figure 11**.

5.2 Colorimetric Detection of Dopamine (DA) in Real Sample:

5.2.1. Human blood serum: To perform the sensing experiment human blood serum was diluted (10 μL serum+90 μL of PBS-7 buffers), next 10 μL diluted serum sample was added to the POD system (Mentioned in section 4). Next, 10 μM of DA was spiked to the resultant

POD system which contained serum also to find out the resultant DA concentration in the serum sample. Before adding the blood serum sample the absorbance of the POD system was recorded. It was found that on adding 10 μL of blood serum sample to the POD system the absorbance at 654 nm was unaffected which shows the presence of negligible concentration of DA in human blood serum. Furthermore, the standard spiking technique was used to find out the concentration of DA in the blood serum sample. For this purpose, 10 μM of DA was spiked three times to the POD system and the resultant absorbance was observed **(Figure 12a).** Next, the resultant absorbance data was matched with the standard linear plot of DA **(Figure 10c)**. Results reflect the presence of almost 0 μM of DA concentration in human blood serum **(Entry 1, Table 4).**

5.2.2. Ripped banana peel: To prepare the sample 10 g of washed fresh ripped banana peel was grinded in 30 mL of PBS buffer (pH-3). Next, the resultant ground mixture was sonicated for 30 minutes to collect as much possible dopamine from the banana peel. Next, the mixture was centrifuged and filtered by using filter paper. The resultant filtrate was further employed as a real sample for the DA sensing. Before adding the banana peel sample the absorbance of the POD system was recorded. It was found that on adding 10 μL of banana peel sample to the POD system the reaction of the absorbance at 654 nm was decreased slightly which shows the presence of dopamine in banana peel. Further, 10 μM of DA was spiked three times and resultant absorbance was observed **(Figure 12b).** Next, the resultant spectra were compared with the standard DA plot **(Figure 10c)** to find out the resultant DA concentration. Interestingly, 0 μM concentration of dopamine was detected in the banana peel sample **(Entry 2, Table 4).**

5.2.3. Dopamine Hydrochloride Injection:

Dopamine hydrochloride injection (Commercial name "Domin" manufactured by Neon Chemical Laboratories India) was purchased from a local market. To perform the sensing experiment a diluted sample was made of total volume 1 mL with 990 μL MilliQ water and 10 μL of pure Domine. After shaking well, the sample was wrapped with aluminium foil to avoid the self-oxidation of dopamine to dopachrome and kept at below 15 ^{o}C. Further, 10 μL of diluted dopamine hydrochloride was added to the POD system as mentioned in previous sections. On adding the sample slight decrease in the UV-vis band was observed at wavelength 652 nm **(Figure 12c).** Interestingly the concentration of DA was detected at 10 μM in the DA injection sample. Afterwards, it was confirmed by using the spiked technique. Standard DA

sample (0, 10, 10, 10 μM) was spiked to the same reaction mixture we got the corresponding resultant DA concentration as summarised in **(Entry 3, Table 4).**

6. Colorimetric Detection of Nitrite: Optimized conditions for the POD-like activity of F-Cu (Described in section 4) were utilized for the colorimetric detection of Nitrite ions. Sodium Nitrite ($NaNO_2$) was used as a standard substrate (10 mM in water) for the detection of NO_2^-. The variable concentrations of sodium nitrite solution (0, 10, 20, 30, 40, 50, 60, 70, 80, 100, 120, 140 μM) were added into the POD system as described in section 4 and incubated at room temperature. The UV-vis absorption spectra displayed a decrease in the 652 nm band with the increase in nitrite concentration. The change in absorbance at 652 nm as a function of nitrite concentrations was plotted and the detection limit of 4 μM was extracted using the same equation as mentioned above **(Table 5)**.

6.1 Interference Experiment for Nitrite Detection: Interference experiment was conducted to demonstrate the sensitivity of our system towards nitrite ions (NO_2^-). Specifically, we aimed to assess whether our system could selectively detect nitrite ions in the presence of various other analytes. For this purpose, we prepared solutions for each analyte at a concentration of 140 μM. This concentration was chosen because it represents the maximum concentration of nitrite ions required to convert the blue-coloured ^{ox}TMB to the yellow-coloured ^{Diazo}TMB system. Along with 140 μM of interfering analyte, 0.2 mM TMB (prepared from a 20 mM stock solution in DMSO), and 0.9 mM hydrogen peroxide (H_2O_2) (from a 50 mM stock solution) were all mixed in phosphate-buffered saline (PBS, 1X) at pH 3.0. Additionally, 200 μL of the F-Cu suspension (1 mg/mL in DMSO) was added to the reaction mixture. After mixing all components to the system, the samples were incubated for 5 minutes. This incubation period was determined to be the minimum time necessary to observe a significant color change and a corresponding change in the absorbance of ^{Diazo}TMB. Interestingly, our results showed that out of all the analytes tested, only the nitrite ions (NO_2^-) induced both a noticeable color change and a decrease in the absorbance of ^{ox}TMB at 652 nm **(Figure 13e).**

6.2 Colorimetric Detection of Nitrite in Real Samples: To perform the detection experiment first we prepared real samples of both carrot and spinach. To make the real samples we followed well-known standard procedure.[7,83] To detect the nitrite (NO_2^-) in real samples standard addition method was employed here. Furthermore, 100 μL of real was added to the POD system as described in previous section 4. After incubating for a few minutes, we started to record the UV-visible spectra of the reaction mixture which shows the change of color from blue to yellow. The maximum absorbance corresponds to sample volume **(Figure 14 a**

and14b) and spiked $NaNO_2$ concertation (μM) was matched with a standard curve as shown in **Figure 13d** and results of detection are shown in **(Table 6)**.

2.5 References

(1) Land, K. J.; Boeras, D. I.; Chen, X.-S.; Ramsay, A. R.; Peeling, R. W. REASSURED Diagnostics to Inform Disease Control Strategies, Strengthen Health Systems and Improve Patient Outcomes. *Nat. Microbiol.* **2018**, *4* (1), 46–54. https://doi.org/10.1038/s41564-018-0295-3.

(2) Zandieh, M.; Liu, J. Nanozymes: Definition, Activity, and Mechanisms. *Adv. Mater.* **2024**, *36* (10), 2211041–2211048. https://doi.org/10.1002/adma.202211041.

(3) Shi, Q.; Song, Y.; Zhu, C.; Yang, H.; Du, D.; Lin, Y. Mesoporous Pt Nanotubes as a Novel Sensing Platform for Sensitive Detection of Intracellular Hydrogen Peroxide. *ACS Appl. Mater. Interfaces* **2015**, *7* (43), 24288–24295. https://doi.org/10.1021/acsami.5b08146.

(4) Mirzaei, Y.; Gholami, A.; Sheini, A.; Bordbar, M. M. An Origami-Based Colorimetric Sensor for Detection of Hydrogen Peroxide and Glucose Using Sericin Capped Silver Nanoparticles. *Sci. Rep.* **2023**, *13* (1), 1–10. https://doi.org/10.1038/s41598-023-34299-1.

(5) Boruah, P. K.; Borthakur, P.; Neog, G.; Le Ouay, B.; Afzal, N. U.; Manna, P.; Das, M. R. Porous Nitrogen-Doped Crumpled Graphene Nanoparticles: A Metal-Free Nanozyme for Selective Detection of Dopamine in Aqueous Medium and Human Serum. *ACS Appl. Nano Mater.* **2023**, *6* (3), 1667–1677. https://doi.org/10.1021/acsanm.2c04582.

(6) Ayala, M.; Torres, E. Peroxidases as Potential Industrial Biocatalysts. In *Heme Peroxidases*; The Royal Society of Chemistry, 2015; pp 309–333. https://doi.org/10.1039/9781782622628-00309.

(7) Liu, J.; Gong, L.; Chen, H.; Gui, J.; Zhu, X.; Liu, M.; Zhang, Y.; Yao, S. Fe-Single-Atom Nanozyme Catalysts for Sensitive and Selective Detection of Nitrite via Colorimetry and Test Strips. *ACS Appl. Nano Mater.* **2023**, *6* (7), 5879–5888. https://doi.org/10.1021/acsanm.3c00253.

(8) Luetic, S.; Knezovic, Z.; Jurcic, K.; Majic, Z.; Tripkovic, K.; Sutlovic, D. Leafy Vegetable Nitrite and Nitrate Content: Potential Health Effects. *Foods* **2023**, *12* (8), 1655. https://doi.org/10.3390/foods12081655.

(9) Kgedal, B.; Goldstein, D. S. Catecholamines and Their Metabolites. *J. Chromatogr. B Biomed. Sci. Appl.* **1988**, *429* (C), 177–233. https://doi.org/10.1016/S0378-4347(00)83871-2.

(10) Su, L.; Qin, S.; Xie, Z.; Wang, L.; Khan, K.; Tareen, A. K.; Li, D.; Zhang, H. Multi-Enzyme Activity Nanozymes for Biosensing and Disease Treatment. *Coord. Chem. Rev.* **2022**, *473*, 214784. https://doi.org/10.1016/j.ccr.2022.214784.

(11) Zhang, X.; Chen, X.; Zhao, Y. Nanozymes: Versatile Platforms for Cancer Diagnosis and Therapy. *Nano-Micro Lett.* **2022**, *14* (1), 1–27. https://doi.org/10.1007/s40820-022-00828-2.

(12) Gao, Y.; Wu, K.; Li, H.; Chen, W.; Fu, M.; Yue, K.; Zhu, X.; Liu, Q. Glutathione

Detection Based on Peroxidase-like Activity of Co3O4–Montmorillonite Nanocomposites. *Sensors Actuators B Chem.* **2018**, *273* (July), 1635–1639. https://doi.org/10.1016/j.snb.2018.07.091.

(13) Poulos, T. L. Heme Enzyme Structure and Function. *Chem. Rev.* **2014**, *114* (7), 3919–3962. https://doi.org/10.1021/cr400415k.

(14) Wei, H.; Wang, E. Nanomaterials with Enzyme-like Characteristics (Nanozymes): Next-Generation Artificial Enzymes. *Chem. Soc. Rev.* **2013**, *42* (14), 6060–6093. https://doi.org/10.1039/c3cs35486e.

(15) Ashrafi, A. M.; Bytesnikova, Z.; Barek, J.; Richtera, L.; Adam, V. Biosensors and Bioelectronics A Critical Comparison of Natural Enzymes and Nanozymes in Biosensing and Bioassays. *Biosens. Bioelectron.* **2021**, *192* (April), 113494. https://doi.org/10.1016/j.bios.2021.113494.

(16) Gao, L.; Zhuang, J.; Nie, L.; Zhang, J.; Zhang, Y.; Gu, N.; Wang, T.; Feng, J.; Yang, D.; Perrett, S.; Yan, X. Intrinsic Peroxidase-like Activity of Ferromagnetic Nanoparticles. *Nat. Nanotechnol.* **2007**, *2* (9), 577–583. https://doi.org/10.1038/nnano.2007.260.

(17) Salarizadeh, N.; Sadri, M.; Sajedi, R. H. Synthesis and Catalytic Evaluation of Fe 3 O 4 /MWCNTs Nanozyme as Recyclable Peroxidase Mimetics: Biochemical and Physicochemical Characterization. *Appl. Organomet. Chem.* **2018**, *32* (2), 1–10. https://doi.org/10.1002/aoc.4018.

(18) Geng, X.; Xie, X.; Liang, Y.; Li, Z.; Yang, K.; Tao, J.; Zhang, H.; Wang, Z. Facile Fabrication of a Novel Copper Nanozyme for Efficient Dye Degradation. *ACS Omega* **2021**, *6* (9), 6284–6291. https://doi.org/10.1021/acsomega.0c05925.

(19) Fang, M.; Zheng, R.; Wu, Y.; Yue, D.; Qian, X.; Zhao, Y.; Bian, Z. CuO Nanosheet as a Recyclable Fenton-like Catalyst Prepared from Simulated Cu(Ii) Waste Effluents by Alkaline H 2 O 2 Reaction. *Environ. Sci. Nano* **2019**, *6* (1), 105–114. https://doi.org/10.1039/c8en00930a.

(20) Makam, P.; Yamijala, S. S. R. K. C.; Bhadram, V. S.; Shimon, L. J. W.; Wong, B. M.; Gazit, E. Single Amino Acid Bionanozyme for Environmental Remediation. *Nat. Commun.* **2022**, *13* (1), 1505. https://doi.org/10.1038/s41467-022-28942-0.

(21) Li, X.; Zhang, Y.; Tan, W.; Jin, P.; Zhang, P.; Li, K. Bioinspired Coassembly of Copper Ions and Nicotinamide Adenine Dinucleotides for Single-Site Nanozyme with Dual Catalytic Functions. *Anal. Chem.* **2023**, *95* (5), 2865–2873. https://doi.org/10.1021/acs.analchem.2c04389.

(22) Banerjee, D.; Vishwakarma, S.; Nayak, M.; Upadhyay, A.; Pradhan, L.; Makam, P.; Mukherjee, S. Fabrication of Zinc-Tryptophan Nanoassemblies for Antibacterial and Wound Healing Applications. *ACS Appl. Nano Mater.* **2025**, *8* (8), 4263–4278. https://doi.org/10.1021/acsanm.5c00657.

(23) Vishwakarma, S.; Tiwari, O. S.; Shukla, R.; Gazit, E.; Makam, P. Amyloid Inspired Single Amino Acid (Phenylalanine)-Based Supramolecular Functional Assemblies: From Disease to Device Applications. *Chem. Soc. Rev.* **2025**, *54* (1), 465–483. https://doi.org/10.1039/D4CS00996G.

(24) Liu, Q.; Kuzuya, A.; Wang, Z. G. Supramolecular Enzyme-Mimicking Catalysts Self-Assembled from Peptides. *iScience* **2023**, *26* (1), 105831.

https://doi.org/10.1016/j.isci.2022.105831.
(25) DİKİCİ, E.; ÖNAL ACET, B.; GÖK, T.; ACET, Ö.; ODABAŞI, M. Self-Assembled Short Peptide Nanostructures: Dipeptides''. *MANAS J. Eng.* **2023**, *11* (1), 83–91. https://doi.org/10.51354/mjen.1282790.
(26) Liu, Q.; Wan, K.; Shang, Y.; Wang, Z. G.; Zhang, Y.; Dai, L.; Wang, C.; Wang, H.; Shi, X.; Liu, D.; Ding, B. Cofactor-Free Oxidase-Mimetic Nanomaterials from Self-Assembled Histidine-Rich Peptides. *Nat. Mater.* **2021**, *20* (3), 395–402. https://doi.org/10.1038/s41563-020-00856-6.
(27) Hamley, I. W. Biocatalysts Based on Peptide and Peptide Conjugate Nanostructures. *Biomacromolecules* **2021**, *22* (5), 1835–1855. https://doi.org/10.1021/acs.biomac.1c00240.
(28) Makam, P.; Yamijala, S. S. R. K. C.; Tao, K.; Shimon, L. J. W.; Eisenberg, D. S.; Sawaya, M. R.; Wong, B. M.; Gazit, E. Non-Proteinaceous Hydrolase Comprised of a Phenylalanine Metallo-Supramolecular Amyloid-like Structure. *Nat. Catal.* **2019**, *2* (11), 977–985. https://doi.org/10.1038/s41929-019-0348-x.
(29) Deng, D.; Novoselov, K. S.; Fu, Q.; Zheng, N.; Tian, Z.; Bao, X. Catalysis with Two-Dimensional Materials and Their Heterostructures. *Nat. Nanotechnol.* **2016**, *11* (3), 218–230. https://doi.org/10.1038/nnano.2015.340.
(30) Tsuneda, T. Fenton Reaction Mechanism Generating No OH Radicals in Nafion Membrane Decomposition. *Sci. Rep.* **2020**, *10* (1), 1–13. https://doi.org/10.1038/s41598-020-74646-0.
(31) Kumar Das, T.; Mondal, A. K.; Tiwari, O. S.; Makam, P.; Leitus, G.; Gazit, E.; Claudio, F.; Naaman, R. Spin-Induced Electron Transmission through Metal-Organic Chiral Crystals. *Phys. Chem. Chem. Phys.* **2023**, *25* (33), 22124–22129. https://doi.org/10.1039/d3cp02579a.
(32) Muir, J. A.; Ortiz, A. Crystal Data for Bis(l-Isoleucinato)Nickel(II) Dihydrate. *J. Appl. Crystallogr.* **1977**, *10* (6), 489–489. https://doi.org/10.1107/S0021889877014034.
(33) Tang, M.; Zhu, B.; Wang, Y.; Wu, H.; Chai, F.; Qu, F.; Su, Z. Nitrogen- and Sulfur-Doped Carbon Dots as Peroxidase Mimetics: Colorimetric Determination of Hydrogen Peroxide and Glutathione, and Fluorimetric Determination of Lead(II). *Microchim. Acta* **2019**, *186* (9). https://doi.org/10.1007/s00604-019-3710-4.
(34) Li, H.; Wen, Y.; Zhu, X.; Wang, J.; Zhang, L.; Sun, B. Novel Heterostructure of a MXene@NiFe-LDH Nanohybrid with Superior Peroxidase-Like Activity for Sensitive Colorimetric Detection of Glutathione. *ACS Sustain. Chem. Eng.* **2020**, *8* (1), 520–526. https://doi.org/10.1021/acssuschemeng.9b05987.
(35) Zhao, Z.; Lin, T.; Liu, W.; Hou, L.; Ye, F.; Zhao, S. Colorimetric Detection of Blood Glucose Based on GOx@ZIF-8@Fe-Polydopamine Cascade Reaction. *Spectrochim. Acta - Part A Mol. Biomol. Spectrosc.* **2019**, *219*, 240–247. https://doi.org/10.1016/j.saa.2019.04.061.
(36) Li, D.; Wu, S.; Wang, F.; Jia, S.; Liu, Y.; Han, X.; Zhang, L.; Zhang, S.; Wu, Y. A Facile One-Pot Synthesis of Hemin/ZIF-8 Composite as Mimetic Peroxidase. *Mater. Lett.* **2016**, *178*, 48–51. https://doi.org/10.1016/j.matlet.2016.04.200.
(37) Xia, F.; Shi, Q.; Nan, Z. Facile Synthesis of Cu-CuFe2O4nanozymes for Sensitive Assay of H2O2and GSH. *Dalt. Trans.* **2020**, *49* (36), 12780–12792.

https://doi.org/10.1039/d0dt02395g.
(38) Wang, Y.; Liu, X.; Wang, M.; Wang, X.; Ma, W.; Li, J. Facile Synthesis of CDs@ZIF-8 Nanocomposites as Excellent Peroxidase Mimics for Colorimetric Detection of H2O2 and Glutathione. *Sensors Actuators, B Chem.* **2021**, *329* (October 2020). https://doi.org/10.1016/j.snb.2020.129115.
(39) Wang, Y.; Wang, M.; Wang, X.; Ma, W.; Liu, J.; Li, J. Designed Synthesis of CD@Cu-ZIF-8 Composites as Excellent Peroxidase Mimics for Assaying Glutathione. *Mater. Chem. Front.* **2021**, *5* (16), 6125–6132. https://doi.org/10.1039/D1QM00702E.
(40) Liu, Q.; Zhu, R.; Du, H.; Li, H.; Yang, Y.; Jia, Q.; Bian, B. Higher Catalytic Activity of Porphyrin Functionalized Co3O 4 Nanostructures for Visual and Colorimetric Detection of H 2O2 and Glucose. *Mater. Sci. Eng. C* **2014**, *43*, 321–329. https://doi.org/10.1016/j.msec.2014.07.032.
(41) Song, Y.; Qu, K.; Zhao, C.; Ren, J.; Qu, X. Graphene Oxide: Intrinsic Peroxidase Catalytic Activity and Its Application to Glucose Detection. *Adv. Mater.* **2010**, *22* (19), 2206–2210. https://doi.org/10.1002/adma.200903783.
(42) Fan, K.; Wang, H.; Xi, J.; Liu, Q.; Meng, X.; Duan, D.; Gao, L.; Yan, X. Optimization of Fe3O4 Nanozyme Activity via Single Amino Acid Modification Mimicking an Enzyme Active Site. *Chem. Commun.* **2017**, *53* (2), 424–427. https://doi.org/10.1039/c6cc08542c.
(43) Xu, B.; Li, S.; Zheng, L.; Liu, Y.; Han, A.; Zhang, J.; Huang, Z.; Xie, H.; Fan, K.; Gao, L.; Liu, H. A Bioinspired Five-Coordinated Single-Atom Iron Nanozyme for Tumor Catalytic Therapy. *Adv. Mater.* **2022**, *34* (15), 1–9. https://doi.org/10.1002/adma.202107088.
(44) Cao, W.; Ju, P.; Wang, Z.; Zhang, Y.; Zhai, X.; Jiang, F.; Sun, C. Colorimetric Detection of H2O2 Based on the Enhanced Peroxidase Mimetic Activity of Nanoparticles Decorated Ce2(WO4)3 Nanosheets. *Spectrochim. Acta Part A Mol. Biomol. Spectrosc.* **2020**, *239*, 118499. https://doi.org/10.1016/j.saa.2020.118499.
(45) Yin, S.-J.; Chen, G.-Y.; Zhang, C.-Y.; Wang, J.-L.; Yang, F.-Q. Zeolitic Imidazolate Frameworks as Light-Responsive Oxidase-like Mimics for the Determination of Adenosine Triphosphate and Discrimination of Phenolic Pollutants. *Microchim. Acta* **2023**, *190* (1), 25. https://doi.org/10.1007/s00604-022-05602-0.
(46) Song, W.; Sun, P.; Zhou, J.; Han, X.; Dai, Q.; Chai, F. The Fabrication of CuBTC@PW 12 with Prominent Peroxidase-Mimicking Activity for Colorimetric Detection of H 2 O 2 and Ascorbic Acid via "on–off" Switch. *New J. Chem.* **2023**, *47* (33), 15721–15730. https://doi.org/10.1039/D3NJ02611F.
(47) Chen, Y.; Zhong, Q.; Wang, Y.; Yuan, C.; Qin, X.; Xu, Y. Colorimetric Detection of Hydrogen Peroxide and Glucose by Exploiting the Peroxidase-like Activity of Papain. *RSC Adv.* **2019**, *9* (29), 16566–16570. https://doi.org/10.1039/C9RA03111A.
(48) Wang, W.; Jiang, X.; Chen, K. CePO4:Tb,Gd Hollow Nanospheres as Peroxidase Mimic and Magnetic–Fluorescent Imaging Agent. *Chem. Commun.* **2012**, *48* (54), 6839. https://doi.org/10.1039/c2cc32328a.
(49) Wang, N.; Sun, J.; Chen, L.; Fan, H.; Ai, S. A Cu2(OH)3Cl-CeO2 Nanocomposite with Peroxidase-like Activity, and Its Application to the Determination of Hydrogen Peroxide, Glucose and Cholesterol. *Microchim. Acta* **2015**, *182* (9–10), 1733–1738.

https://doi.org/10.1007/s00604-015-1506-8.
(50) Ding, Y.; Yang, B.; Liu, H.; Liu, Z.; Zhang, X.; Zheng, X.; Liu, Q. FePt-Au Ternary Metallic Nanoparticles with the Enhanced Peroxidase-like Activity for Ultrafast Colorimetric Detection of H2O2. *Sensors Actuators, B Chem.* **2018**, *259*, 775–783. https://doi.org/10.1016/j.snb.2017.12.115.
(51) Lee, G.; Kim, C.; Kim, D.; Hong, C.; Kim, T.; Lee, M.; Lee, K. Multibranched Au–Ag–Pt Nanoparticle as a Nanozyme for the Colorimetric Assay of Hydrogen Peroxide and Glucose. *ACS Omega* **2022**, *7* (45), 40973–40982. https://doi.org/10.1021/acsomega.2c04129.
(52) Yang, H.; Zha, J.; Zhang, P.; Xiong, Y.; Su, L.; Ye, F. Sphere-like CoS with Nanostructures as Peroxidase Mimics for Colorimetric Determination of H2O2 and Mercury Ions. *RSC Adv.* **2016**, *6* (71), 66963–66970. https://doi.org/10.1039/c6ra16619a.
(53) Socaci, C.; Pogacean, F.; Biris, A. R.; Coros, M.; Rosu, M. C.; Magerusan, L.; Katona, G.; Pruneanu, S. Graphene Oxide vs. Reduced Graphene Oxide as Carbon Support in Porphyrin Peroxidase Biomimetic Nanomaterials. *Talanta* **2016**, *148*, 511–517. https://doi.org/10.1016/j.talanta.2015.11.023.
(54) Liu, Q.; Tang, P.; Xing, X.; Cheng, W.; Liu, S.; Lu, X.; Zhong, L. Colorimetry /SERS Dual-Sensor of H2O2 Constructed via TMB–Fe3O4@ AuNPs. *Talanta* **2022**, *240* (August 2021), 123118. https://doi.org/10.1016/j.talanta.2021.123118.
(55) Ding, Y.; Liu, H.; Gao, L.-N.; Fu, M.; Luo, X.; Zhang, X.; Liu, Q.; Zeng, R.-C. Fe-Doped Ag2S with Excellent Peroxidase-like Activity for Colorimetric Determination of H2O2. *J. Alloys Compd.* **2019**, *785*, 1189–1197. https://doi.org/10.1016/j.jallcom.2019.01.225.
(56) Zhang, C.-Y.; Peng, L.-J.; Chen, G.-Y.; Zhang, H.; Yang, F.-Q. Investigation on the Peroxidase-like Activity of Vitamin B6 and Its Applications in Colorimetric Detection of Hydrogen Peroxide and Total Antioxidant Capacity Evaluation. *Molecules* **2022**, *27* (13), 4262. https://doi.org/10.3390/molecules27134262.
(57) Dong, S.; Xi, J.; Wu, Y.; Liu, H.; Fu, C.; Liu, H.; Xiao, F. High Loading MnO 2 Nanowires on Graphene Paper: Facile Electrochemical Synthesis and Use as Flexible Electrode for Tracking Hydrogen Peroxide Secretion in Live Cells. *Anal. Chim. Acta* **2015**, *853* (1), 200–206. https://doi.org/10.1016/j.aca.2014.08.004.
(58) Lee, J. H.; Huynh-Nguyen, B.-C.; Ko, E.; Kim, J. H.; Seong, G. H. Fabrication of Flexible, Transparent Silver Nanowire Electrodes for Amperometric Detection of Hydrogen Peroxide. *Sensors Actuators B Chem.* **2016**, *224*, 789–797. https://doi.org/10.1016/j.snb.2015.11.006.
(59) Yang, H.; Zha, J.; Zhang, P.; Xiong, Y.; Su, L.; Ye, F. Sphere-like CoS with Nanostructures as Peroxidase Mimics for Colorimetric Determination of H 2 O 2 and Mercury Ions. *RSC Adv.* **2016**, *6* (71), 66963–66970. https://doi.org/10.1039/C6RA16619A.
(60) Li, F.; Yu, X.-H.; Kong, F.-Y.; Wang, Z.-X.; Wang, W. Incorporating Doped Carbon Nanodots and Metal Ions as an Excellent Artificial Peroxidase for H 2 O 2 Detection. *RSC Adv.* **2017**, *7* (50), 31281–31286. https://doi.org/10.1039/C7RA05146H.
(61) Wen, X.; Long, M.; Tang, A. Flake-like Cu 2 O on TiO 2 Nanotubes Array as an

Efficient Nonenzymatic H 2 O 2 Biosensor. *J. Electroanal. Chem.* **2017**, *785*, 33–39. https://doi.org/10.1016/j.jelechem.2016.12.018.

(62) Wang, T.; Tian, J.; Li, T.; Li, J. Enzyme Properties and Thermal Stability of Horseradish Peroxidase (HRP-DL). In *Proceedings of the 2016 International Conference on Engineering and Technology Innovations*; Atlantis Press: Paris, France, 2016; pp 227–231. https://doi.org/10.2991/iceti-16.2016.40.

(63) Zhu, Y.; Yang, Z.; Chi, M.; Li, M.; Wang, C.; Lu, X. Synthesis of Hierarchical Co3O4@NiO Core-Shell Nanotubes with a Synergistic Catalytic Activity for Peroxidase Mimicking and Colorimetric Detection of Dopamine. *Talanta* **2018**, *181* (December 2017), 431–439. https://doi.org/10.1016/j.talanta.2018.01.019.

(64) Reza Hormozi Nezhad, M.; Tashkhourian, J.; Khodaveisi, J.; Reza Khoshi, M. Simultaneous Colorimetric Determination of Dopamine and Ascorbic Acid Based on the Surface Plasmon Resonance Band of Colloidal Silver Nanoparticles Using Artificial Neural Networks. *Anal. Methods* **2010**, *2* (9), 1263–1269. https://doi.org/10.1039/c0ay00302f.

(65) Yin, M.; Li, S.; Wan, Y.; Feng, L.; Zhao, X.; Zhang, S.; Liu, S.; Cao, P.; Wang, H. A Selective Colorimetric Strategy for Probing Dopamine and Levodopa through the Mussel-Inspired Enhancement of Fe3O4 Catalysis. *Chem. Commun.* **2019**, *55* (80), 12008–12011. https://doi.org/10.1039/c9cc06211d.

(66) Elugoke, S. E.; Fayemi, O. E.; Adekunle, A. S.; Mamba, B. B.; Nkambule, T. T. I.; Ebenso, E. E. Electrochemical Sensor for the Detection of Dopamine Using Carbon Quantum Dots/Copper Oxide Nanocomposite Modified Electrode. *FlatChem* **2022**, *33* (December 2021). https://doi.org/10.1016/j.flatc.2022.100372.

(67) Aparna, T. K.; Sivasubramanian, R.; Dar, M. A. One-Pot Synthesis of Au-Cu2O/RGO Nanocomposite Based Electrochemical Sensor for Selective and Simultaneous Detection of Dopamine and Uric Acid. *J. Alloys Compd.* **2018**, *741*, 1130–1141. https://doi.org/10.1016/j.jallcom.2018.01.205.

(68) Plowman, B. J.; Mahajan, M.; O'Mullane, A. P.; Bhargava, S. K. Electrochemical Detection of Dopamine and Cytochrome c at a Nanostructured Gold Electrode. *Electrochim. Acta* **2010**, *55* (28), 8953–8959. https://doi.org/10.1016/j.electacta.2010.08.045.

(69) Zhu, J.; Peng, X.; Nie, W.; Wang, Y.; Gao, J.; Wen, W.; Selvaraj, J. N.; Zhang, X.; Wang, S. Hollow Copper Sulfide Nanocubes as Multifunctional Nanozymes for Colorimetric Detection of Dopamine and Electrochemical Detection of Glucose. *Biosens. Bioelectron.* **2019**, *141* (June), 111450. https://doi.org/10.1016/j.bios.2019.111450.

(70) Wang, J.; Huang, R.; Qi, W.; Su, R.; He, Z. Preparation of Amorphous MOF Based Biomimetic Nanozyme with High Laccase- and Catecholase-like Activity for the Degradation and Detection of Phenolic Compounds. *Chem. Eng. J.* **2022**, *434* (October 2021), 134677. https://doi.org/10.1016/j.cej.2022.134677.

(71) Baron, R.; Zayats, M.; Willner, I. Dopamine-, L-DOPA-, Adrenaline-, and Noradrenaline-Induced Growth of Au Nanoparticles: Assays for the Detection of Neurotransmitters and of Tyrosinase Activity. *Anal. Chem.* **2005**, *77* (6), 1566–1571. https://doi.org/10.1021/ac048691v.

(72) Hayat, A.; Cunningham, J.; Bulbul, G.; Andreescu, S. Evaluation of the Oxidase like Activity of Nanoceria and Its Application in Colorimetric Assays. *Anal. Chim. Acta* **2015**, *885*, 140–147. https://doi.org/10.1016/j.aca.2015.04.052.

(73) Kim, D.-S.; Kang, E.-S.; Baek, S.; Choo, S.-S.; Chung, Y.-H.; Lee, D.; Min, J.; Kim, T.-H. Electrochemical Detection of Dopamine Using Periodic Cylindrical Gold Nanoelectrode Arrays. *Sci. Rep.* **2018**, *8* (1), 14049. https://doi.org/10.1038/s41598-018-32477-0.

(74) Seto, D.; Maki, T.; Soh, N.; Nakano, K.; Ishimatsu, R.; Imato, T. A Simple and Selective Fluorometric Assay for Dopamine Using a Calcein Blue-Fe2+ Complex Fluorophore. *Talanta* **2012**, *94*, 36–43. https://doi.org/10.1016/j.talanta.2012.02.025.

(75) Liang, W.; Yang, M. Urbanization, Economic Growth and Environmental Pollution: Evidence from China. *Sustain. Comput. Informatics Syst.* **2019**, *21*, 1–9. https://doi.org/10.1016/j.suscom.2018.11.007.

(76) Kaur, B.; Pandiyan, T.; Satpati, B.; Srivastava, R. Simultaneous and Sensitive Determination of Ascorbic Acid, Dopamine, Uric Acid, and Tryptophan with Silver Nanoparticles-Decorated Reduced Graphene Oxide Modified Electrode. *Colloids Surfaces B Biointerfaces* **2013**, *111*, 97–106. https://doi.org/10.1016/j.colsurfb.2013.05.023.

(77) Shukla, R. P.; Aroosh, M.; Matzafi, A.; Ben-Yoav, H. Partially Functional Electrode Modifications for Rapid Detection of Dopamine in Urine. *Adv. Funct. Mater.* **2021**, *31* (17). https://doi.org/10.1002/adfm.202004146.

(78) Kim, Y. R.; Bong, S.; Kang, Y. J.; Yang, Y.; Mahajan, R. K.; Kim, J. S.; Kim, H. Electrochemical Detection of Dopamine in the Presence of Ascorbic Acid Using Graphene Modified Electrodes. *Biosens. Bioelectron.* **2010**, *25* (10), 2366–2369. https://doi.org/10.1016/j.bios.2010.02.031.

(79) Li, J.; Yang, J.; Yang, Z.; Li, Y.; Yu, S.; Xu, Q.; Hu, X. Graphene–Au Nanoparticles Nanocomposite Film for Selective Electrochemical Determination of Dopamine. *Anal. Methods* **2012**, *4* (6), 1725. https://doi.org/10.1039/c2ay05926f.

(80) Slivka, A.; Cohen, G. Hydroxyl Radical Attack on Dopamine. *J. Biol. Chem.* **1985**, *260* (29), 15466–15472. https://doi.org/10.1016/S0021-9258(17)36277-4.

(81) Liu, X.; Liu, J. Biosensors and Sensors for Dopamine Detection. *View* **2021**, *2* (1), 1–16. https://doi.org/10.1002/VIW.20200102.

(82) Kanazawa, K.; Sakakibara, H. High Content of Dopamine, a Strong Antioxidant, in Cavendish Banana. *J. Agric. Food Chem.* **2000**, *48* (3), 844–848. https://doi.org/10.1021/jf9909860.

(83) Wang, M.; Liu, P.; Zhu, H.; Liu, B.; Niu, X. Ratiometric Colorimetric Detection of Nitrite Realized by Stringing Nanozyme Catalysis and Diazotization Together. *Biosensors* **2021**, *11* (8), 1–15. https://doi.org/10.3390/bios11080280.

(84) Adegoke, O.; Zolotovskaya, S.; Abdolvand, A.; Daeid, N. N. Rapid and Highly Selective Colorimetric Detection of Nitrite Based on the Catalytic-Enhanced Reaction of Mimetic Au Nanoparticle-CeO2 Nanoparticle-Graphene Oxide Hybrid Nanozyme. *Talanta* **2021**, *224* (November 2020). https://doi.org/10.1016/j.talanta.2020.121875.

(85) Nam, J.; Jung, I.-B.; Kim, B.; Lee, S.-M.; Kim, S.-E.; Lee, K.-N.; Shin, D.-S. A Colorimetric Hydrogel Biosensor for Rapid Detection of Nitrite Ions. *Sensors Actuators*

B Chem. **2018**, *270*, 112–118. https://doi.org/10.1016/j.snb.2018.04.171.

(86) Pan, Y.; Jiang, J.; Kan, X. Diazo-Reaction Based Dual-Mode Colorimetric-Electrochemical Sensing of Nitrite in Pickled Food. *Analyst* **2023**, *148* (19), 4869–4876. https://doi.org/10.1039/D3AN01196H.

(87) Manea, F.; Remes, A.; Radovan, C.; Pode, R.; Picken, S.; Schoonman, J. Simultaneous Electrochemical Determination of Nitrate and Nitrite in Aqueous Solution Using Ag-Doped Zeolite-Expanded Graphite-Epoxy Electrode. *Talanta* **2010**, *83* (1), 66–71. https://doi.org/10.1016/j.talanta.2010.08.042.

(88) Liu, Y.; Gu, H. Y. Amperometric Detection of Nitrite Using a Nanometer-Sized Gold Colloid Modified Pretreated Glassy Carbon Electrode. *Microchim. Acta* **2008**, *162* (1–2), 101–106. https://doi.org/10.1007/s00604-007-0946-9.

(89) Chen, L. H.; Zang, J. B.; Wang, Y. H.; Bian, L. Y. Electrochemical Oxidation of Nitrite on Nanodiamond Powder Electrode. *Electrochim. Acta* **2008**, *53* (8), 3442–3445. https://doi.org/10.1016/j.electacta.2007.12.023.

(90) Da Silva, S.; Cosnier, S.; Almeida, M. G.; Moura, J. J. G. An Efficient Poly(Pyrrole-Viologen)-Nitrite Reductase Biosensor for the Mediated Detection of Nitrite. *Electrochem. commun.* **2004**, *6* (4), 404–408. https://doi.org/10.1016/j.elecom.2004.02.007.

(91) Marlinda, A. R.; Pandikumar, A.; Yusoff, N.; Huang, N. M.; Lim, H. N. Electrochemical Sensing of Nitrite Using a Glassy Carbon Electrode Modified with Reduced Functionalized Graphene Oxide Decorated with Flower-like Zinc Oxide. *Microchim. Acta* **2015**, *182* (5–6), 1113–1122. https://doi.org/10.1007/s00604-014-1436-x.

(92) Zhao, S.; Zhang, K.; Sun, Y.; Sun, C. Hemoglobin/Colloidal Silver Nanoparticles Immobilized in Titania Sol–Gel Film on Glassy Carbon Electrode: Direct Electrochemistry and Electrocatalysis. *Bioelectrochemistry* **2006**, *69* (1), 10–15. https://doi.org/10.1016/j.bioelechem.2005.09.004.

(93) Page, S. E.; Arnold, W. A.; McNeill, K. Terephthalate as a Probe for Photochemically Generated Hydroxyl Radical. *J. Environ. Monit.* **2010**, *12* (9), 1658–1665. https://doi.org/10.1039/c0em00160k.